HHS Public Access

Author manuscript

Cell. Author manuscript; available in PMC 2020 July 25.

Published in final edited form as:

Cell. 2019 July 25; 178(3): 653–671.e19. doi:10.1016/j.cell.2019.06.034.

A Paranigral VTA Nociceptin Circuit that Constrains Motivation for Reward

Kyle E. Parker[1], **Christian E. Pedersen**[1,2], **Adrian M. Gomez**[1], **Skylar M. Spangler**[1,3], **Marie C. Walicki**[1], **Shelley Y. Feng**[1], **Sarah L. Stewart**[1], **James M. Otis**[4], **Ream Al-Hasani**[1,5,6,7], **Jordan G. McCall**[1,5,6,7], **Kristina Sakers**[8,9], **Dionnet L. Bhatti**[1], **Bryan A. Copits**[1], **Robert W. Gereau**[1], **Thomas Jhou**[10], **Thomas J. Kash**[11], **Joseph D. Dougherty**[8,9], **Garret D. Stuber**[4,12,13], **Michael R. Bruchas**[1,2,7,9,14,15]

[1]Departments of Anesthesiology, Division of Basic Research, Anatomy and Neurobiology, and Washington University Pain Center, Washington University School of Medicine, Saint Louis, MO, USA

[2]Department of Biomedical Engineering, Washington University in St. Louis, Saint Louis, Missouri 63130, USA.

[3]Neuroscience Program (DBBS), Washington University School of Medicine, Saint Louis, MO, USA.

[4]Department of Psychiatry, University of North Carolina, Chapel Hill, NC, USA.

[5]Department of Pharmaceutical and Administrative Sciences, St. Louis College of Pharmacy, Saint Louis, MO, USA.

[6]Center for Clinical Pharmacology, St. Louis College of Pharmacy and Washington University School of Medicine, Saint Louis, MO, USA.

[7]Division of Biology and Biomedical Sciences, Washington University School of Medicine, Saint Louis, MO, USA.

[8]Department of Genetics, Washington University School of Medicine, Saint Louis, MO, USA.

[9]Department of Psychiatry, Washington University School of Medicine, Saint Louis, MO, USA.

[10]Department of Neuroscience, Medical University of South Carolina, Charleston, SC, USA.

Correspondence: mbruchas@uw.edu.

Author Contributions

K.E.P., C.E.P. and A.M.G. designed and performed experiments, collected and analyzed data, and wrote the manuscript. C.E.P. collected and analyzed photometry data. S.M.S., M.C.W., S.Y.F. and R.A. performed experiments and collected data. J.M.O, J.G.M., and B.A.C designed and performed in vitro whole cell recordings. R.W.G. helped design and oversee cell recordings. K.S. and D.L.B. designed and performed TRAP experiments and RNA sequencing. J.D.D helped design and oversee TRAP experiments. M.R.B., G.D.S., T.J.K., and T.J. facilitated resources for generation of the *Pnoc*-Cre mouse line. M.R.B. helped design, analyze, oversaw experiments, provided resources, and helped to write the manuscript.

Declaration of Interests

The authors declare no competing interests.

[11]Department of Pharmacology and Bowles Center for Alcohol Studies, School of Medicine, University of North Carolina, Chapel Hill, NC, USA.

[12]Neuroscience Center, University of North Carolina, Chapel Hill, NC, USA.

[13]Department of Cell Biology and Physiology, University of North Carolina, Chapel Hill, NC, USA.

[14]New Address: Department of Anesthesiology and Pain Medicine, Department of Pharmacology, Center for the Neurobiology of Addiction, Pain, and Emotion, University of Washington, Seattle, WA, USA.

[15]Lead Contact

Summary

Nociceptin and its receptor are widely distributed throughout the brain in regions associated with reward behavior, yet how and when they act is unknown. Here we dissected the role of a nociceptin peptide circuit in reward seeking. We generated a *prepronociceptin* (*Pnoc*)-Cre mouse line that revealed a unique subpopulation of paranigral ventral tegmental area (pnVTA) neurons enriched in *prepronociceptin*. Fiber photometry recordings during progressive ratio operant behavior revealed pnVTA^{Pnoc} neurons become most active when mice stop seeking natural rewards. Selective pnVTA^{Pnoc} neuron ablation, inhibition and conditional VTA nociceptin receptor (NOPR) deletion increased operant responding, revealing that the pnVTA^{Pnoc} nucleus and VTA NOPR signaling are necessary for regulating reward motivation. Additionally, optogenetic and chemogenetic activation of this pnVTA^{Pnoc} nucleus caused avoidance and decreased motivation for rewards. These findings provide insight into neuromodulatory circuits that regulate motivated behaviors through identification of a previously unknown neuropeptide-containing pnVTA nucleus that limits motivation for rewards.

Graphical Abstract

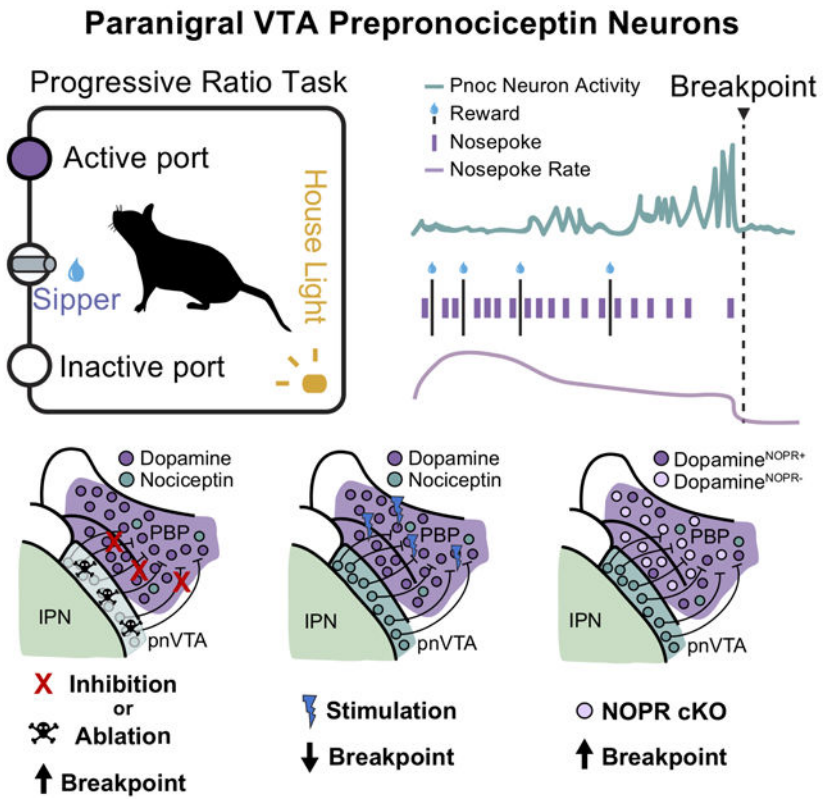

In Brief

A subnuclei of the VTA that expresses the neuropeptide prepronociceptin functions to constrain motivation when the effort to obtain a reward increases

Introduction

Neural circuits that underlie reward seeking are regulated by homeostatic states and adapt to reward availability. Animals are less motivated to seek rewards in environments where resources are scarce (Salamone et al., 2009; Kobayashi and Schultz, 2008). Persistence to seek uncertain rewards can be disadvantageous due to risky exposure to predators or from energy expenditure. To prevent aberrant seeking behavior, neural mechanisms constrain motivation to seek rewards. In humans, deficits within these regulatory processes can manifest into behavioral dysfunctions including depression, addiction, and feeding disorders (Russo and Nestler, 2013; Volkow et al., 2011). In particular, disruption in dopaminergic activity is implicated in the dysregulation of reward seeking and consumption (Morales and Margolis, 2017; Stauffer et al., 2016; Salamone et al., 2009). Evidence suggests heterogeneity of neuronal subtypes and anatomical localization in the VTA, including transmitter and neuropeptide systems that can modulate dopaminergic outputs (Morales and Margolis, 2017; van Zessen et al., 2012; Tan et al., 2012; Jhou et al., 2009). However, how specific neuropeptides regulate motivation through the VTA remains an underexplored area.

Efforts to understand the anatomical basis and specificity of reward regulation by neuropeptides has provided converging evidence that presents the nociceptin (N/OFQ) / nociceptin opioid peptide receptor (NOPR) system as a reward-related neuropeptide system (Castro and Bruchas, 2019; Der-Avakian et al., 2017; Toll et al., 2016; Ozawa et al., 2015; Norton et al., 2002; Zheng et al., 2002; Mollereau and Mouledous, 2000; Mollereau et al., 1994). This opioid system has been proposed to have an endogenous role in regulating motivational state; however, how this regulation may occur remains unresolved. NOPR is broadly expressed in tyrosine hydroxylase (TH)-positive neurons (Norton et al., 2002) and NOPR activation negatively regulates DA neuron activity (Zheng et al., 2002), yet the behavioral consequences of this neuropeptide system's impact in the VTA are unknown. Anatomical studies highlight this system spans multiple reward-related brain nuclei including nucleus accumbens (NAc), striatum, bed nucleus of stria terminalis (BNST), central amygdala (CeA), hypothalamus, hippocampus, and the VTA (Maidment et al., 2002; Ciccocioppo et al., 2000; Mollereau and Mouledous, 2000; Darland et al., 1998; Anton et al., 1996). Pharmacological evidence has suggested that NOPR stimulation can reduce reward-related behaviors, including food consumption and preference for drugs of abuse (Witkin et al., 2014; Zaveri, 2011; Zhao et al, 2003; Kotlinska et al, 2002; Ciccocioppo et al., 2000). Thus, understanding the mechanisms by which this neuropeptide system modulates reward behavior provides essential circuit-based mechanisms for endogenous VTA regulation, and how opioid peptides in this critical structure impact motivation.

To address a possible link between endogenous nociceptin systems and regulation of reward and motivation, we determined if VTA-projecting neurons expressing the precursor gene for nociceptin, prepronociceptin (*Pnoc*), are able to gate reward-related behaviors. First, we generated a prepronociceptin (*Pnoc*)-IRES-Cre knock-in mouse line, implemented retrograde tracing, and identified an enriched *Pnoc*+ neuronal nucleus within the border of the ventral VTA and interpeduncular nucleus (pnVTA) that projects into lateral portions of the VTA. Neural activity recordings revealed that VTA nociceptin neuron activity increases as mice reduce their effort to obtain rewards. This led to the hypothesis that pnVTA^{Pnoc} neurons may regulate motivation for rewards, and that the pnVTA^{Pnoc} neurons could bi-directionally alter motivation to seek rewards. Deletion and inhibition of pnVTA^{Pnoc} neurons dramatically increased breakpoints to obtain reward whereas optogenetic and chemogenetic stimulation of VTA *Pnoc* inputs decreased the breakpoints for rewards. We also report that reward seeking is reduced by nociceptin release and NOPR's action specifically on VTA DA neurons, while the deletion of VTA NOPR or DA neuron NOPR increased reward seeking. Collectively, our findings demonstrate a previously unknown population of pnVTA^{Pnoc} neurons positioned to constrain motivation for rewards via specific neuropeptide signaling on DA neurons in the VTA. The identification and interrogation of this pnVTA nociceptin system provides critical insight into the cell types that limit and regulate motivated behavior.

Results

Anatomical Identification of Endogenous *Pnoc*-expressing VTA Inputs

To virally target nociceptin-containing neurons that project into the VTA, we generated a *prepronociceptin*-IRES-Cre mouse (*Pnoc*-Cre). A targeted knock-in was used to generate a

bicistronic transcript with an IRES to conserve *Pnoc* expression while providing Cre expression under control of the endogenous locus (see Taniguchi et al., 2011) (Figure S1A). We crossed *Pnoc*-Cre mice to the tdTomato flox-stop reporter line (Ai9 and Ai14) (Madisen et al., 2010) as well as the channelrhodopsin2-eYFP reporter line (Ai32) (Figures 1A-B, **see** Methods). These *Pnoc*-Cre^{tdTomato} and *Pnoc*-Cre$^{ChR2/eYFP}$ lines provided a map for *Pnoc*-expressing cells and axonal projections. Using these new mouse lines, we observed an abundance of *Pnoc*-containing cells within the VTA, BNST, CeA, septum, and DG (Figures 1C-E, S1C-D), demonstrating concordance with prior ISH data. We next validated the fidelity of the *Pnoc*-Cre mouse line by fluorescent *in situ* hybridization (FISH) co-labeling of *Pnoc* and Cre in known *Pnoc*-enriched regions. We observed strong Cre-fidelity in the *Pnoc*-Cre mouse line, where FISH shows that *Pnoc* and Cre substantial overlap in *Pnoc*+ mice in multiple brain areas (BNST, CeA, and VTA), whereas Cre is absent in wildtype littermate mice (Figure S1C). While the majority of these brain regions project to the VTA, it was not known if these projections are specifically *Pnoc*-expressing.

To identify putative *Pnoc*+ VTA-projecting brain regions we utilized two retrograde tracing approaches. First, to survey potential projections interacting with DA neurons, we injected a mixture of AAV1-EF1α-DIO-TVA-mCherry: AAV1-EF1α-DIO-RG into the lateral VTA of *DAT*-Cre mice followed by an injection SADΔG-GFP (EnvA, rabies) 20 days later (Tian et al., 2016; Watabe-Uchida et al., 2012). Here, we identified multiple sources of monosynaptic inputs onto VTA DA neurons. Of particular interest was the dense labeling in ventral portions of the VTA, particularly in the paraintrafasciular (PIF) and paranigral nucleus (PN) (Figure 1F, S1F). This area showed robust GFP labeling without helper virus (mCherry), suggesting that local VTA *Pnoc* cells may connect directly onto VTA DA neurons as we observed robust *Pnoc* expression patterns within the paranigral VTA (Figure 1A-C). To confirm this observation, we performed *in situ* hybridization for *Pnoc* and GFP following this rabies tracing approach (Figure 1F). Here we visualized GFP and *Pnoc* co-labeling in the pnVTA (Figure 1E, S1G) suggesting *Pnoc*-expressing neurons have synaptic inputs onto DA (*DAT*-Cre+) cells. To further examine connectivity of this nucleus with the VTA, we injected a retroAAV2-EF1α-DIO-hChR2-(H134R)-eYFP (Tervo et al., 2016), into the lateral VTA of *Pnoc*-Cre mice and visualized eYFP-labeled ChR2+ expressing neurons within the pnVTA. Additionally, we performed in situ hybridization for *Pnoc* and DAT and found that the majority of pnVTA^{Pnoc} neurons do not express *DAT* (Figure S1J-K). Together, these data support the conclusion that *Pnoc*-expressing neurons in the pnVTA synapse onto VTA DA neurons.

Pnoc+ VTA Inputs are Engaged During Low-Yield Reward-Seeking

To determine if VTA^{Pnoc} neurons are active during reward seeking, we recorded the intracellular calcium dynamics (Pologruto et al., 2004) of VTA^{Pnoc} neurons and their terminals in the VTA. We used fiber photometry (Gunaydin et al., 2014) while mice performed an operant task to receive sucrose reward (Figure 2B, 2C). Mice were injected with 400 nl of AAV-DJ-EF1α-DIO-GCaMP6s unilaterally into the pnVTA and implanted with a 400mm optical fiber in the VTA (Figure 2A). Mice were food restricted and underwent Pavlovian conditioning to associate a house light (CS) with access to a sucrose sipper (US). Mice were trained on fixed ratio (FR) operant schedules to nosepoke for 10%

sucrose under an FR1 and then under a FR3 schedule. Following FR3 testing, mice were put through a progressive ratio (PR) test, a task that directly measures the breakpoint at which an animal is unwilling to further work for reward (Hodos, 1961; Richardson and Roberts, 1996). Here, nosepoke criterion exponentially increases for each subsequent reward during the task. Neural activity was recorded during the final FR3 day and the PR test day for two training cycles. Typical baseline drift was observed over the hour-long recording sessions and corrected using standard methods (Parker et al., 2016; Gunaydin et al., 2014) (Figure S2A-C). We found that *Pnoc*+ neural activity in the VTA increased phasically when mice were nosepoking in both FR3 and PR tasks (Figure 2E). Mice nosepoke at a consistent rate throughout the FR3 task, yet in the PR task, mice initially poke at a higher rate, and progressively reduce their poke rate as rewards became more difficult to attain (Figure 2F). Further, evidence shows that VTA DA cells are engaged during operant reward seeking and DA cells are particularly active when effort is high-yield and rewards are attained at a high rate (Gan, Walton, and Phillips, 2010; Hamid et al., 2016; Oliva and Wanat, 2019). To determine how pnVTA^{Pnoc} neurons are active during low and high-yield reward seeking, we analyzed *Pnoc*+ neural activity during nosepoke epochs for different states of PR task performance. To quantify nosepoke-aligned *Pnoc*+ neural activity, mean fluorescence was assessed in 2-second time bins centered on nosepoke events. All peri-nosepoke activity is shown in Figure 2H for individual PR sessions, where each colored pixel represents mean neural activity for an individual active nosepoke. Peri-nosepoke activity was consistently above baseline for nosepokes into the active and inactive ports for the FR3 and PR tasks (Figure 2D). Assessing nosepoke-aligned activity during PR task performance revealed that activity was initially low during nosepokes early in the PR task when rewards were readily attainable. However, activity increased later in the PR session as more nosepokes were required for each subsequent reward. Interestingly, activity was highest during animals' final nosepokes before reaching breakpoint and ceasing reward seeking (Figure 2G, 2I, S2F). Activity was also examined relative to the rate of nosepoking. Nosepoke rate was calculated as the total number of active nosepokes occurring within a 1-minute window centered around a given nosepoke event. Peri-nosepoke activity was at its minimum during high rates of nosepoking when mice were seeking rewards vigorously and increased as the poke rate diminished throughout the PR session (Figure 2J). Altogether, these findings indicate that *Pnoc*+ VTA inputs are engaged during reward seeking, and this activity is negatively correlated to the value of effort. Notably, *Pnoc*+ neural activity returned to baseline several seconds after an animal ceases its reward-seeking behavior (Figure 2I). These data support the conclusion that VTA *Pnoc*+ neurons are engaged during low-yield reward seeking, rather than active in the absence of reward anticipation.

Distinct Populations of VTA^{Pnoc} Neurons are Engaged During Reward Consumption

We also analyzed the activity of VTA^{Pnoc} neurons during other behavioral epochs to offer a comprehensive evaluation of these unique neurons' responsivity. We found a divergence in VTA *Pnoc*+ neural activity during reward consumption between two distinct groups of mice (Figure 3D and 3G). Analysis of optical fiber placement with matched recordings revealed anatomically distinct neural activity during consumption. Mice with anterior optical fibers implanted over pnVTA (anterior to −3.5 AP) had increased activity during reward consumption in FR3 and PR tasks (Figure 3E and 3F) while mice implanted in posterior

VTA (posterior to −3.5 AP) had decreased neural activity during reward consumption in FR3 and PR tasks (Figure 3H and 3I). However, analysis revealed that *Pnoc*+ VTA inputs for both groups of mice had increased activity as mice reduced their rate of reward seeking (Figure 2G and 2J) and that there was no significant effect of fiber placement location and PR task progress in determining peri-nosepoke activity (Figure S2E). This suggests VTA^{Pnoc} neurons and their fiber terminals in the anterior and posterior VTA are engaged similarly during nosepoking for reward but diverge in their neural activity during reward consumption.

Further, VTA^{Pnoc} activity was also recorded in a Pavlovian conditioning paradigm (Figure 3J). The cue was presented 6 seconds before the sipper to allow for dissociation of *Pnoc*+ neural activity during reward anticipation from neural activity during reward consumption. A parallel group of *DAT*-Cre mice (n=7) were also recorded from in an identical Pavlovian paradigm to allow for direct comparison of DA cell activity and *Pnoc*+ cell activity within the VTA in this task. Anterior pnVTA^{Pnoc} cells increased their activity during reward consumption while posterior VTA^{Pnoc} inputs decreased their activity during reward consumption (Figure 3K). Additionally, anterior pnVTA^{Pnoc} cells had decreased activity in response to a reward-predictive cue while posterior VTA^{Pnoc} inputs showed no significant change from baseline during the cue period. Anterior pnVTA^{Pnoc} cells also had sharply increased activity after the end of the 20 second reward period for Pavlovian and operant sessions (Figure 3E and 3K). Reward omission trials were also tested with CS presentation, but no US access (Figure 3J). The consumption-related activity of anterior and posterior VTA^{Pnoc} inputs was absent during the omission trials (Figure 3M) despite mice remaining near the sipper port during extinction (Figure 3L). Lick rate during reward was lowest during Pavlovian conditioning, higher for the FR3 task, and highest for the PR task (Figure 3C). For both anatomically and functionally distinct *Pnoc*+ VTA inputs, the intensity of fluorescence during reward corresponds to lick rate (Pearson's correlation: $r = 0.849$, $p^* = 0.033$) and is negligible when mice are not consuming reward during omission trials (Figure 3B). Although anterior pnVTA^{Pnoc} cells decrease activity during reward anticipation, they did not exhibit any signal that parallels reward prediction error signals associated with reward omission (Schultz et al., 1997, 2007; Hart et al., 2014). However, these neurons are indeed recruited when access to sucrose reward is taken away during the post-reward period (Figure 3B). Altogether, these findings suggest that pnVTA^{Pnoc} cells act to limit seeking behavior, but do not likely represent error in reward anticipation.

pnVTA^{Pnoc} Neurons are Molecularly Heterogeneous

To determine whether pnVTA^{Pnoc} neuron form monosynaptic inputs onto VTA DA neurons, we performed whole-cell electrophysiology of *Pnoc*^{ChR2} neurons within the VTA (Figure 4A, 4E). We found near 100% spike fidelity for all ChR2-eYFP expressing neurons at frequencies of 1, 5, 10, 20, and 40Hz (Figure 4B). (Figure 4C-D) In these neurons optical stimulation evoked robust inhibitory postsynaptic currents (oeIPSCs) in putative dopaminergic cells (IH+) and putative non-dopaminergic (IH−) neurons (Neuhoff et al., 2002). oeIPSCs latency was faster, as well as larger, in IH+ neurons when compared to IH− neurons (Figure 4G-H). We determined that these oeIPSCs inputs to be GABAergic as the oeIPSCs were abolished by blockade of GABA receptors via Gabazine, while unaffected by blockade of glutamate receptors via DNQX (Figure 4I-K). Although, these data suggest a

role for GABA within the VTA^{Pnoc} neuron population, anatomical and photometry data warranted further investigation of their molecular and anatomical identity. Specifically, we conducted a transcriptomic survey of pnVTA^{Pnoc} neuron gene expression using Translating Ribosome Affinity Purification (TRAP) (Sakers, et al, 2017; Mulvey et al., 2018). We injected a Cre-dependent TRAP AAV into the pnVTA of *Pnoc*-Cre mice to selectively tag (Figure S4D) and isolate ribosome-bound mRNA from *Pnoc*+ neurons and performed TRAP followed by RNAseq (Figure 4L-N). We validated TRAP isolation with robust enrichment of *Pnoc* as well as a host of other GPCR and neuropeptide mRNAs in these neurons (see Figure 4N, S4N, Table S2). Notably, we detected expression of both *vGLUT2* (vesicular glutamate transporter) and *vGAT* (vesicular GABA transporter), indicating presence of pnVTA^{Pnoc} neurons containing both glutamate and/or GABA. FISH for *Pnoc*+, *vGAT*, and *vGLUT2* revealed that anterior pnVTA^{Pnoc} cells predominantly co-express *vGLUT2* and the relative prevalence of *Pnoc/vGAT* coexpression increased toward posterior VTA expressing *Pnoc* neurons (Figure 4J-L, S4A-B), demonstrating that there are two distinct, overlapping *Pnoc*+ subpopulations. *Pnoc* colocalization with either *vGAT* or *vGLUT2* appears to form "pockets" where pnVTA^{Pnoc} cells are strictly glutamatergic while PBP *Pnoc* cells are GABAergic. Furthermore, injection of AAV5-EF1α-DIO-ChR2-eYFP injection into *vGAT*-Cre or *vGLUT2*-Cre revealed distinct expression patterns as compared to the pnVTA^{Pnoc} cells (Figure S4E-F). Together, these data indicate that pnVTA^{Pnoc} neurons have GABAergic connectivity with DA cells, but these pnVTA^{Pnoc} neurons are also heterogeneous in anatomical location and transcriptomic identity.

Selective Ablation and Inhibition of pnVTA^{Pnoc} Neurons Enhances Reward Seeking Breakpoint

To determine the functional necessity of the pnVTA^{Pnoc} neurons in regulating natural reward-seeking behavior, we utilized three separate, but parallel approaches to assess if deletion or inhibition of pnVTA^{Pnoc} neurons impacts motivation for rewards. First, we injected an AAV5-FLEX-taCasp3-TEVp into the pnVTA of *Pnoc*-Cre+ and *Pnoc*-Cre− mice to induce apoptosis in Cre-positive pnVTA^{Pnoc} neurons. This caused a significant loss in pnVTA^{Pnoc} neurons of *Pnoc*+ mice (Figure 5C-D, S5A). We observed that pnVTA^{Pnoc} neuron ablation increased responding under the PR task showing increases in total nosepokes, rewards received, as well as robust increases in operant responding across the entire PR test (Figure 5B,E-F, S5B-E). These manipulations increased breakpoint and seeking for reward (FR3) but did not impact reward consumption (i.e. lick rate) (Figure S5F). Taken together, these data demonstrate that selective removal of pnVTA^{Pnoc} neurons enhances PR responding for sucrose, implicating a necessary role for these unique pnVTA neurons in limiting motivation for rewards.

We injected virus encoding the inhibitory DREADD receptor (AAV5-hSyn-DIO-hM4Di-mCherry into the pnVTA of *Pnoc*-Cre+ and *Pnoc*-Cre− mice (Figure 5G and 5H) and tested mice in a PR task following the administration of two CNO doses: 1mg/kg (i.p.) and 5mg/kg (i.p.) (Figure 5G). We found that chemogenetic inhibition of pnVTA^{Pnoc} neurons significantly increased nosepoke responding following CNO (5 mg/kg) and increased the number rewards received following both CNO doses (1 and 5 mg/kg) (Figure 5I, 5H, S5G and S5H). However, the above approaches do not assess how inhibiting pnVTA^{Pnoc} neurons

during specific epochs of the behavioral task might modulate the motivation to obtain natural rewards. Therefore, in a parallel series of experiments, we injected an AAV5-EF1α-DIO-eNpHR3.0-eYFP, and chronically implanted bilateral fiber optics into their terminal region of the lateral VTA of *Pnoc*-Cre^{+} and *Pnoc*-Cre^{-} mice (Figure 5K-L). We then assessed whether motivation to obtain sucrose rewards was altered by time-locked photoinhibition of pnVTA^{Pnoc} neurons during nosepoking or licking. Photoinhibition of pnVTA^{Pnoc} neurons was found to increase the total number of nosepokes and the number of total rewards during the PR task, but only when inhibition was paired to nosepoking behavior (Figure 5M-N, S5I-J). These data suggest that pnVTA^{Pnoc} neurons are necessary for operant responding for rewards, but not for consumption of a natural reward. Taken together, these data demonstrate that selective removal and inhibition of pnVTA^{Pnoc} neurons robustly enhances PR responding, implicating a key role for these neurons in regulating low-yield reward-seeking behavior.

Optogenetic and Chemogenetic Stimulation of pnVTA^{Pnoc} Neurons Decreases Effort to Receive a Natural Reward and Promotes Aversion

To determine the sufficiency of pnVTA^{Pnoc} neurons in modulating sucrose reward seeking, we injected AAV5-EF1α-DIO-ChR2-eYFP, and chronically implanted a fiber optic into their terminal region of the lateral VTA of *Pnoc*-Cre+ and *Pnoc*-Cre− mice (Figure 6_A-B, S1A-B). During the PR task, mice received 60 minutes of 5Hz photo-stimulation or had the photo-stimulation time-locked (10Hz, 1 sec) to either their nosepoking or licking. We found that 5Hz stimulation of *Pnoc*+ VTA neurons and their terminals significantly decreased total nosepokes and rewards during FR3 and PR tests (Figure 6C-F, Figure S6E-F). We also determined whether the selective NOPR antagonist, J-113397, (3mg/kg, i.p.) would block this reduction in behavior. Indeed, antagonist administration prevented the photo-stimulated pnVTA^{Pnoc}-mediated suppression of sucrose seeking (Figure 6G), suggesting that tonic stimulation of pnVTA^{Pnoc} neurons releases NOPR agonist nociceptin. Time-locked stimulation did not affect sucrose seeking behaviors (Figure S6C), yet we found that nosepoke-paired stimulation led to either diminished (n = 7) or enhanced (n = 4) sucrose seeking (Figure S6D). These data suggest that while continuous, tonic unpaired pnVTA^{Pnoc} stimulation reduces PR performance, behavior-paired acute stimulation results in a divergent responding during the task, underscoring the additional complex features of this unique population within the pnVTA.

We next determined whether selective stimulation of pnVTA^{Pnoc} neurons causes a particular valence response (Namburi et al., 2016). We injected AAV5-DIO-EF1α-ChR2-eYFP into the pnVTA of *Pnoc*-Cre+ or *Pnoc*-Cre− mice and used a real-time place test (RTPT) paradigm (Figure 6H) to determine whether mice prefer or avoid neutral contexts paired with various photostimulation frequencies (0-60hz) (Al-Hasani et al., 2015). We found that photostimulation of pnVTA^{Pnoc} neurons (5Hz and 10Hz) produced significant real-time avoidance behavior (Figure S6H-I). This real time avoidance behavior is reversible, conserved following multiple test days, as well as within test (ON-OFF-ON), as demonstrated in Figure 6I.

In a parallel series of experiments, we determined the effects of stimulating pnVTA^{Pnoc} neurons via excitatory (hM3Gq) chemogenetic manipulation. We injected AAV5-hSyn-DIO-hM3Dq-mCherry into the pnVTA region of *Pnoc*-Cre+ and *Pnoc*-Cre− mice (Figure 6J) and tested mice in the PR task following CNO administration (1 and 5mg/kg, i.p.) We found that chemogenetic stimulation (5mg/kg CNO) of pnVTA^{Pnoc} neurons decreased operant responding and the number of rewards received during the PR task (Figure 6K-L, Figure S6K-L). In fact, we also found that CNO administration dose-dependently (1mg/kg and 5mg/kg) decreased the total number of nosepokes and the total number of sucrose rewards received in *Pnoc*-Cre$^{hM3D(Gq)}$ expressing mice (Figure 6M, Figure S6M). Both 1mg and 5mg CNO doses reduced operant responding and subsequent reward received only in *Pnoc*-Cre$^{hM3D(Gq)}$ expressing mice (Figure 6G-6H). Nosepoke responses and rewards for *Pnoc*-Cre$^{hM3D(Gq)}$ mice treated with CNO + the NOPR antagonist J-113397 returned to similar levels as compared to mice following vehicle administration (Figure 6M, Figure S6M). These results demonstrate a reversal of CNO-induced reduction in PR responding and further indicate that stimulating pnVTA^{Pnoc} neurons releases nociceptin to act on NOP receptors.

We next determined whether stimulation of pnVTA^{Pnoc} neurons integrates salient negative affective information with associated environmental cues. Here we injected AAV5-hSyn-DIO-hM3Dq-mCherry in *Pnoc*-Cre+ and *Pnoc*-Cre− mice and measured conditioned place preference (CPP) for the context paired with DREADD agonist CNO (Figure 6N). We observed that repeated administration of CNO (5 mg/kg, i.p.) in a paired context induced a robust conditioned place aversion (CPA) only in *Pnoc*-Cre$^{hM3D(Gq)}$ mice (Figure 6O-P), without impacting locomotor activity, (Figure S6N). These data indicate that pnVTA^{Pnoc} neuron activation drives aversion in neutral environments and integrates negative valence with relevant contextual stimuli.

VTA NOPR Expression is Necessary and Sufficient for Constraining Reward Seeking

Our results above demonstrated involvement of both the neuropeptide nociceptin and NOPR in regulating sucrose seeking behavior; however, how and where these NOPR-mediated effects act is unknown. We next determined whether VTA NOPR expression is necessary and sufficient to coordinate this behavior. Using wildtype and NOPR knockout (KO) mice, we examined how selective NOPR agonist SCH-221510 administration impacts reward seeking within the PR task (Figure 7A). Here, we found that SCH-221510 administration (10mg/kg, i.p.) significantly reduced the number of nosepokes and rewards compared to baseline PR responding of wildtype mice, while having no significant effect in NOPR$^{-/-}$ mice (Figure 7B), complimenting previous experimental pnVTA^{Pnoc} manipulation results in Figure 6..Additionally, the administration NOPR agonist had no effect on the average lick rate during sucrose consumption (Figure 7C). This data indicates that exogenous NOPR stimulation is sufficient to reduce breakpoints for reward.

Next, to determine how and where NOPR mediates these effects on reward-seeking behavior, we recorded calcium transients in DA neurons in the VTA during pavlovian behavior following selective NOPR manipulation. In this experiment, *DAT*-Cre mice were injected with AAV-DJ-EF1α-DIO-GCaMP6s unilaterally into the VTA and implanted with

optical fiber in the medial-lateral VTA (Figure 7D). Mice were trained in a Pavlovian conditioning task as described in Figure 3J. Mice were either injected with vehicle, SCH-221015 (10 mg/kg, i.p.), or J-113,397 (3 mg/kg, i.p.) prior to *in vivo* photometry recording of DA neuron activity during responding to cue and sucrose rewards (Figure 7A, S7C-E). NOPR activation significantly reduced overall baseline DA neural activity, while NOPR blockade increased baseline activity as compared to vehicle treated groups. This bidirectional effect was observed during consumption, but not during cue presentation (Figure 7E-G). Despite the effects on DA cell activity, there were no differences in lick rate or consumption of sucrose across treatments (Figure S7D). These data suggest that NOPR impacts DA neuron excitability during reward behavior.

To determine the necessity of NOPR expression specifically within the VTA on motivation and reward-seeking behavior, we further examined these behaviors following VTA-specific conditional deletion of NOPR. We first generated an original conditional NOPR knockout mouse (Figure S7A-B) in order to selectively remove NOPR from regions and cell-types of interest. Here, we bilaterally injected 350nl of AAV5-PGK-Cre or AAV9-rTH-PI-Cre-SV40 virus (for selective DA neuron expression) into the VTA of $NOPR^{lox/lox}$ (labeled NOPR cKO and $NOPR^{TH\text{-}Cre}$, respectively) and control mice (Figure 7H). Using the same operant training and testing paradigms, we found that NOPR KO, VTA^{NOPR} cKO, and VTA $NOPR^{TH\text{-}Cre}$ cKO mice had significantly higher nosepokes and rewards received during operant responding as compared to littermate controls (Figure 7I). Similar to mice that have had $pnVTA^{Pnoc}$ ablation or inhibition of pnVTA neurons (Figure 5), these NOPR KO, VTA^{NOPR} cKO, and VTA $NOPR^{TH\text{-}Cre}$ cKO mice showed a significant increase in responding for sucrose during the PR task (Figure 7J). Although, VTA NOPR cKO mice consumed more sucrose during the PR task, there was no difference in the average lick rate during reward consumption as a result of this manipulation (Figure S7F-G). Furthermore, to characterize this regional KO of NOPR, we used *in situ* hybridization for NOPR in VTA slices and found a significant reduction of NOPR mRNA expression in DA neurons (24±1.6%) in Cre-injected $NOPR^{lox/lox}$ mice, while leaving NOPR expression intact (99±0.7%) in control mice (Figure 7K-L). Additionally, VTA $NOPR^{TH\text{-}Cre}$ cKO mice show a significant reduction in NOPR expression as revealed by immunofluorescence of Cre in DA neurons (97±0.6%) and NOPR expression in DA neurons (20.3±3.3%) in rTH-PI-Cre-injected $NOPR^{lox/lox}$ mice (Figure 7M-N).

To determine the sufficiency of NOPR in VTA DA neurons to produce these effects on reward seeking, we generated a mouse line of constitutive NOPR KO mice crossed to a *Th*-Cre mouse line (Figure 7O). We then constructed an AAV5-EF1α-DIO-NOPR-eYFP virus and injected it into the VTA of $NOPR^{-/-}$ x TH-Cre+ mice to express NOPR only within VTA DA neurons (Figure 7O-P). We then trained these mice as in previous experiments and examined how the selective NOPR agonist SCH-221510 (10 mg/kg, i.p.) impacted PR responding for sucrose in mice that express NOPR only in VTA DA neurons. Here we found that SCH-221510 significantly reduced responding in $NOPR^{-/-}$::$^{NOPR\text{-}VTA}$ mice, while leaving control (AAV5-EF1α-DIO-eYFP) animal responding was unaffected (Figure 7Q, S7I). This selective VTA DA NOPR expression and agonist stimulation did not alter lick rate or impact locomotor activity (Figure S7J-K). These results indicate a critical role for

endogenous nociceptin and NOPR activity on DA neurons. Together these data strongly support the conclusion that VTA NOPR activation constrains motivation to seek rewards.

DISCUSSION

We generated a *Pnoc*-Cre mouse line to specifically target and isolate *Pnoc*-expressing inputs into the VTA and map endogenous sources of nociceptin. Following examination of *Pnoc* expression patterns in two new *Pnoc* reporter lines (Figure 1) we identified numerous brain regions rich in *Pnoc*-expressing neurons. Considering our data indicating monosynaptic inputs onto VTA DA neurons, we investigated multiple potential neurobiological sources of nociceptin inputs into the VTA, and found that the pnVTA not only expressed a distinct pattern of nociceptin neuron labeling, but was also comprised of likely dense inputs onto VTA DA neurons. Considering that the VTA and other ventral midbrain nuclei contain heterogeneous neuronal populations, no studies to date have demonstrated the function of this unique *Pnoc*-containing neuron population within the pnVTA region.

When examining the activity of pnVTA^{Pnoc} neurons during reward seeking conditions, we found they have relatively low activity when rewards are readily accessible and effort requirements are low during the PR task or during reward anticipation in Pavlovian conditioning tasks. These neurons are dynamically engaged during higher PR levels when mice are nosepoking infrequently for reward and not achieving sipper access (Figure 2G). In fact, we find that neural activity is highest when mice are reaching their breakpoint and terminate their reward-seeking behavior. Distinct activation of pnVTA^{Pnoc} neurons was also observed directly after the reward period when the sucrose sipper retracted and mice could no longer consume the reward. Although pnVTA^{Pnoc} neurons are very active when current reward access is removed, they surprisingly did not exhibit any significant signal associated with reward prediction errors that have been canonically observed in DA cells within the VTA (Figure 3B). This is a surprising finding as DA cells phasically increase firing in response to reward predictive cues in anticipation of reward and are also dramatically suppressed when expected rewards are not received (Schultz et al., 1997; Hart et al., 2014). Together, the endogenous activity of pnVTA^{Pnoc} neurons indicates that they do not signal errors in reward prediction, but rather signal to limit the motivation for reward. Indeed, mesolimbic DA is necessary for potentiating reward-seeking behavior when the effort required for reward is greater and the rate of reward attainment is lower, while DA activity is lower when future rewards are uncertain and the effort to reward payout ratio is greater (Gan, Walton, and Phillips, 2010; Hamid et al., 2016). Here we report that the pnVTA^{Pnoc} neurons are increasingly active as nosepoke rate declines and likely inhibit VTA DA neurons during low-yield reward seeking via release of nociception and subsequent NOPR activation. It is possible that pnVTA^{Pnoc} neurons increasingly suppress DA neuron tonic activity to diminish and regulate seeking for less attainable rewards.

Given endogenous pnVTA^{Pnoc} activity during reward seeking, we hypothesized that these neurons contribute inhibitory tone during sucrose seeking to limit motivation. Indeed, we observed increased PR performance following chronic ablation or inhibition of pnVTA^{Pnoc} neurons. Interestingly, PR performance also increased when inhibition of pnVTA^{Pnoc}

neurons was time-locked only to nosepoke events (Figure 5K-5N). These data suggest that pnVTA^{Pnoc} neurons terminate seeking behavior particularly when the effort to obtain the reward increases. Accordingly, continuous pnVTA^{Pnoc} neuron stimulation reduced PR performance indicating that enhanced pnVTA^{Pnoc} activity is sufficient to diminish the pursuit of natural rewards, while NOPR antagonist administration reversed this effect. It was uncertain whether this loss in motivation is due to the promotion of a negative affective state or the enhancement of an existing inhibitory tone that coordinates the intersection of reward value and effort. pnVTA^{Pnoc} neuron stimulation resulted in active avoidance during real-time stimulation and mice avoided stimulation-paired environmental stimuli within the CPP assay. These data are indicative of a neuronal population that also promotes a negative affective state. Interestingly, this data parallels other studies that demonstrate that mice avoid VTA DA neuron inhibition (Tan et al., 2012; Danjo et al., 2014). pnVTA ^{Pnoc} neurons are likely positioned to receive input related to affective stimuli that subsequently drive inhibitory tone onto local VTA DA neuron populations, which would translate into reduced motivation in reward contexts and a negative affective state in non-reward contexts.

To further characterize this unique VTA^{Pnoc} population, we also assessed the activity of these neurons under a variety of reward epochs and behaviors. Examination of VTA^{Pnoc} activity during the reward access period and anatomical analysis of fiber optic placement location within the VTA revealed two additional discrete activity patterns during reward consumption; increased *Pnoc* neuron activity in the pnVTA and a suppression of activity in the posterior VTA. This bimodal population response may be due to the activation of a network of neurons that respond specifically to sucrose consumption. Indeed, it is known that posterior RMTG GABAergic inputs to the VTA are suppressed during reward consumption (Hong et al., 2011). It is possible that there are two *Pnoc*+ VTA input populations that are engaged during reward consumption: one posterior GABAergic pathway that is inhibited and one anterior glutamatergic pathway that is excited. In fact, our histological data show that the pnVTA^{Pnoc} neurons in anterior VTA predominantly express glutamatergic (Figure 4) markers. Recent work by Root et al. (2018) revealed that a majority VTA VGlut2-expressing neurons' activity increases in response to aversive stimuli and decreases in response to rewarding stimuli. However, they also report other subpopulations that respond to different behaviorally relevant conditions. These are characteristics that we also observe within our cell population, as sucrose consumption enhances pnVTA^{Pnoc} neuron activity, while stimulation of pnVTA^{Pnoc} neurons drives aversion. Interestingly, our electrophysiological results revealed primarily GABAergic *Pnoc* neuron monosynaptic connectivity to putative DA neurons (Figure 4I-K). Although this establishes a subpopulation of GABA-containing *Pnoc* neurons within the VTA, the distinct pattern of expression we observed within the pnVTA was preserved throughout all viral infection experiments as described here and is indicative of an anterior, predominantly glutamatergic, population of pnVTA^{Pnoc} neurons. Specifically, we propose a distinct glutamatergic *Pnoc* population that is medial and ventral to DA neurons and a GABAergic *Pnoc* population that lies more lateral and dorsal to the VTA (Figure 4P-Q). In addition, TRAP RNAseq transcriptomic analysis revealed that pnVTA^{Pnoc} neurons are enriched in a number of unique receptors, transmitters, and peptides, including vGLUT2 (*slc17a6*), neurotensin-1 receptor (*NTSR1*), and orexin-1 receptor (*HCRTR1*) (Figure 4M-N). The enrichment of these

specific genes within these neurons is of particular interest as these genes are also found within some VTA DA neurons (Baimel et al., 2015; Binder et al., 2001). Considering this data, pnVTA^{Pnoc} neurons may receive input from hypothalamic areas that help to coordinate reward motivation. This activity may provide feedback to VTA DA neurons to coordinate the intersection of reward value and reward-seeking action, however these hypotheses require future circuit-based experiments.

Recent studies have demonstrated that monoamine nuclei including the VTA, dorsal raphe, and locus coeruleus have a diverse host of neuronal populations based on their anatomical localization and projection target (Matthews et al., 2016; Seo et al, 2016; Beier et al, 2015). However, prior studies (Morales and Margolis, 2017) have yet to determine the connectivity and/or function of critical neuropeptide producing neurons in the VTA. Further investigation of VTA neuropeptide and neurotransmitter heterogeneity using intersectional genetic methods will elucidate how the VTA coordinates complex inputs to shape motivated behavior.

Given the concomitant intersection of results that indicate a unique pnVTA^{Pnoc} population regulates reward seeking by nociceptin release, we further determined whether there is a critical, necessary role for NOPR within the VTA in maintaining normal reward seeking. Global NOPR KO and conditional NOPR deletion from VTA DA cells dramatically enhanced reward-seeking behaviors in a manner similar to pnVTA^{Pnoc} neuron ablation and inhibition (Figure 5). This data indicates that, along with our electrophysiological and tracing studies, the action of pnVTA^{Pnoc} neurons on reward seeking is mediated through NOPR activation on dopaminergic VTA neurons. Interestingly, fiber photometry recordings of VTA DA activity during Pavlovian conditioning revealed that agonist activation of NOPR suppressed baseline DA neural activity. Phasic DA activity in response to the reward-predictive cue was left largely intact during NOPR activation while persistent DA activity during reward consumption was suppressed. This suggests that VTA NOPR activation may selectively limit PR performance by dramatically shifting dopaminergic tone. This finding is further supported by pnVTA^{Pnoc} manipulation affecting effort for reward, but not the rate of reward consumption. Lastly, we demonstrated that the conditional rescue and stimulation of NOPR specifically in VTA DA neurons greatly diminishes breakpoint responding. These data demonstrate the effectiveness of NOPR stimulation in inhibiting seeking for sucrose when it is exclusively expressed and stimulated in VTA DA neurons. Collectively, these data support a unique role of intra-VTA nociceptin release and subsequent NOPR activation acting to dynamically constrain DA neuron activity during reward-seeking behavior. In our case, an absent VTA nociceptin or NOPR system allows higher breakpoints for obtaining rewards in which a normally functioning NOPR system would typically engage and regulate appropriate reward seeking under various environmental conditions through DA neuron inhibition.

Our findings present a previously unknown pnVTA cell population of nociceptin-containing neurons that are positioned to suppress reward seeking via localized peptidergic action on NOPR-expressing VTA dopamine neurons. Understanding how this discrete pnVTA nucleus is critical to the regulation of motivation provides essential insights into the diverse behavioral functions of the VTA. How local VTA regions and neuropeptides are functionally

defined at the circuit, cellular, and molecular level reveals insights into how the VTA coordinates homeostatic motivational balance during dysregulated motivational states like depression and addiction.

STAR Methods

CONTACT FOR REAGENT AND RESOURCE SHARING

Additional information and requests for resources and reagents should be directed to and will be fulfilled by the Lead Contact, Michael Bruchas (mbruchas@uw.edu).

EXPERIMENTAL MODEL AND SUBJECT DETAILS

Animals—Adult (20–35g) male and female prepronociceptin-IRES-Cre (*Pnoc*-Cre), NOPR KO, NOPR cKO mice were group housed, given access to food pellets and water ad libitum, and maintained on a 12 hr: 12 hr light:dark cycle (lights on at 7:00 AM). All mice were kept in a sound-attenuated, isolated holding facility in the lab one week prior to surgery, post-surgery, and throughout the duration of the behavioral assays to minimize stress. For ablation, chemogenetic, and optogenetic experiments, we used Cre- cage and littermate controls. For NOPR KO and NOPR cKO behavioral experiments, experimental mice were compared to age-matched wildtype controls. Unless otherwise noted, animals had ad libitum access to food and water. The mice were bred at Washington University in Saint Louis by crossing the *Pnoc*-Cre mice, NOPR KO, and NOPR cKO with C57BL/6 wild-type mice and backcrossed for seven generations. Additionally, where needed, *Pnoc*-Cre mice were then crossed to Ai9-tdTomato and Ai32-ChR2-eYFP mice on C57BL/6 background, bred, and backcrossed for seven generations. For the generation of NOPRlox/lox mice, Exon 4 of NOPR was flanked on both sides by loxP sites. All animals were drug and test naive, individually assigned to specific experiments as described, and not involved with other experimental procedures. Student's t-tests did not detect any statistically significant difference when comparing animals grouped by sex, therefore male and female mice were combined to complete final group sizes. All animals were monitored for health status daily and before experimentation for the entirety of the study. All procedures were approved by the Animal Care and Use Committee of Washington University in St. Louis and performed in accordance with the National Institute of Health's guide for the care and use of laboratory animals.

Generation of *Pnoc*-IRES-Cre mouse line—129 BAC genomic clones containing the Pnoc genes was used to target a cassette containing the Cre recombinase gene preceded by an internal ribosomal entry sequence (IRES-Cre) downstream of the *Pnoc* stop codon, so as to have endogenous *Pnoc* genes drive Cre recombinase expression. The *Pnoc*-IRES-Cre targeting constructs were electroporated into W4 ES cells and screened using an FRT-flanked neo-cassette. Targeted clones were injected into blastocysts. Chimeras were obtained and bred for germline transmission of the *Pnoc*-IRES-Cre allele. Following germline transmission, *Pnoc*-IRES-cre mice were crossed to Rosa-FLPR mice to remove the neo cassette at the 3′end of the IRES-cre sequence.

METHOD DETAILS

Tissue processing—Unless otherwise stated, animals were transcardially perfused with 0.1 M phosphate-buffered saline (PBS) and then 40 mL 4% paraformaldehyde (PFA). Brains were dissected and post-fixed in 4% PFA overnight and then transferred to 30% sucrose solution for cryoprotection. Brains were sectioned at 30 μM on a microtome and stored in a 0.01M phosphate buffer at 4°C prior to immunohistochemistry and tracing experiments. For behavioral cohorts, viral expression and optical fiber placements were confirmed before inclusion in the presented datasets.

Immunohistochemistry—Immunohistochemistry was performed as previously described by (Al-Hasani et al., 2013; Kim et al., 2013; McCall et al., 2015). In brief, mice were intracardially perfused with 4% paraformaldehyde, and then brains were sectioned (30μm) and placed in 0.1 M PB until immunohistochemistry. Free-floating sections were washed in 0.1 M PBS for 3 × 10 minutes intervals. Sections were then placed in blocking buffer (0.5% Triton X-100 and 5% natural goat serum in 0.1 M PBS) for 1 hr at room temperature. After blocking buffer, sections were placed in primary antibody (chicken anti-tyrosine hydroxylase,1:2000, Aves Labs, Inc.; rabbit anti-nociceptin, 1:500, abcam) overnight at room temperature. After 3 × 10-minute 0.1 M PBS washes, sections were incubated in secondary antibody (AlexaFluor 488 goat anti-rabbit; AlexaFluor 594 or 633 goat anti-chicken, Life Technologies) for 2 hours at room temperature, followed by subsequent washes (3 X 10 minute in 0.1 M PBS). Later, sections were incubated in NeuroTrace (435/455 blue fluorescent Nissl stain, ThermoFisher Scientific) for 1 hour, followed by 3 × 10 minute 0.1 MPBS then 3 × 10-minute 0.1 M PB washes. After immunostaining, sections were mounted and coverslipped with Vectashield HardSet mounting medium (Vector Laboratories) and imaged on a Leica TCS SPE confocal microscope.

RNAscope Fluorescent In Situ Hybridization (FISH)—Following rapid decapitation of mice, brains were flash frozen in −50°C 2-methylbutane and stored at −80°C for further processing. Coronal sections containing the BNST, CeA, and VTA/IPN regions, corresponding to the injection plane used in the behavioral experiments, were cut at 20μM at −20°C and thaw-mounted onto Super Frost Plus slides (Fisher). Slides were stored at −80°C until further processing. FISH was performed a ccording to the RNAScope® 2.0 Fluorescent Multiplex Kit for Fresh Frozen Tissue (Advanced Cell Diagnostics, Inc.) as described by Wang et al., 2012. Slides containing the specified coronal brain sections were fixed in 4% paraformaldehyde, dehydrated, and pretreated with protease IV solution for 30 mins. Sections were then incubated for target probes for mouse *Pnoc*, (accession number NM_010932.2, probe region 325-1263), VGlut (*slc17a6*, accession number NM_080853.3, probe region 1986-2998), VGat (*slc32a1*, accession number NM_009508.2, probe region 894-2037), Cre (accession number KC845567.1, probe region 1058-2032), NOPR (accession number NM_011012.5, probe region 988-1937, TH (accession number NM_009377.1, probe region 483 – 1603), DAT (*slc6a3*, accession number NM_010020.3, probe region 1486-2525) and GFP (accession number AF275953.1, probe region 12-686) for 2 hrs. All target probes consisted of 20 ZZ oligonucleotides and were obtained from Advanced Cell Diagnostics. Following probe hybridization, sections underwent a series of probe signal amplification steps (AMP1-4) including a final incubation of fluorescently

labeled probes (Alexa 488, Atto 550, Atto 647), designed to target the specified channel (C1-C3 depending on assay) associated with the probes. Slides were counterstained with DAPI and coverslips were mounted with Vectashield Hard Set mounting medium (Vector Laboratories). Images were obtained on a Leica TCS SPE confocal microscope (Leica), and Application Suite Advanced Fluorescence (LAS X) and ImageJ/Fiji software were used for analyses. Images for *Pnoc* Cre+ and *Pnoc* Cre− mice for quantification of *Pnoc* / Cre coexpression were carried out under the same standards (i.e. intensity, threshold, exposure time for each slide). To analyze the images, each image was opened in ImageJ software using the "Color Threshold" function, selecting the default threshold method and RGB color space. Within the threshold window, the default the settings were kept consistent for each slide. After adjusting for fluorescence threshold, we counted the total pixels of the fluorescent signal, assuming that each pixel represents a single molecule of RNA as per RNAscope's methodology. A positive cell consisted of an area within the radius of a DAPI nuclear staining that measured at least 10 total positive pixels and an integrated density of >5. Three separate slices from the BNST, CeA, and pnVTA were used for each animal and that total is reflected in the data (n = 4).

Stereotaxic viral / optical fiber implant surgeries—After the mice were acclimated to the holding facility for at least seven days, the mice were anaesthetized in an induction chamber (1-4% isoflurane) and placed into a stereotaxic frame (Kopf Instruments, Model 1900) where they were maintained at 1-2% isoflurane. Mice were then injected unilaterally or bilaterally, depending on experimental paradigm, using a blunt needle (86200, Hamilton Company) at a rate of 100 nL / min. The type of virus, injection volume, and stereotaxic coordinates for each experiment are listed in Supplementary Table 1. Mice were allowed to recover for five weeks prior to behavioral testing, permitting optimal expression of the virus. For optogenetic experiments, one week prior to behavioral testing, intracranial optic fiber implants were directed above the VTA (AP −3.15, ML ± 0.5, DV −4.25). Implants were secured using at least two bone screws and a dental cement headcap (Lang Dental).

Generation of TRAP virus—The TRAP construct (eGFP/Rpl10a), a generous gift from N. Heintz lab, was PCR cloned into a commercial Gateway compatible entry vector (pENTR-3C), sequenced to confirm coding sequence, then transferred into an AAV-EF1α-DIO-Gateway destination vector using LR-clonase (Invitrogen) and following the manufacture's protocol (Heiman et al., 2008). AAV-EF1α-DIO-Gateway plasmid was previously generated by replacing Chr2-eYfp from AAV-EF1α-DIO-ChR2-eYFP with an ATTR flanked Gateway acceptor cassette. The resulting AAV-EF1α-DIO-TRAP Plasmid was maxiprepped, sequence confirmed, then packaged by UNC Vector Core using standard protocols. Cre dependence was confirmed anatomically in independent mice and TRAP construct showed cytoplasmic and nucleolar localization within cells consistent with incorporation into ribosomes.

TRAP RNAseq Assay—TRAP was carried out as described in Sakers et al., 2017. Briefly, a 1mm coronal slice was dissected 6mm caudal to the base of the olfactory bulbs. Five slices (across 5 mice) were pooled and homogenized in cold lysis buffer (10 mM HEPES [pH 7.4], 150 mM KCl, 5 mM MgCl2, 0.5 mM dithiothreitol, 100 μg/ml

cycloheximide, protease inhibitors, and recombinant RNase inhibitors) using a Teflon-glass homogenizer and a power drill. Homogenates were spun at 2,000xg for 10 minutes, and the resulting supernatant was lysed with 30mM DHPC and 1% NP40 followed by incubation on ice for 15 minutes. The lysate was then cleared at 20,000xg for 20 minutes, and the resulting supernatant was applied to EGFP-coated magnetic beads. 10% of this input was kept for a 'Pre-IP' sample. Immunoprecipitations were carried out for 4 hours at 4C with constant rotation. Four 1mL washes were carried out with wash buffer (10 mM HEPES [pH 7.4], 350 mM KCl, 5 mM MgCl2, 1% NP-40, 0.5mM dithiothreitol, 100 μg/ml cycloheximide and recombinant RNase inhibitors). RNA extraction using Trizol LS was carried out followed by Zymo RNA clean and concentrator-5 kit, with DNAse treatment, according to manufacturer's guidelines.

Library Prep and Sequencing: cDNA was made and amplified from 1ng of RNA using the Ovation RNA Amplification System V2 from NuGEN. cDNA was sheared to ~200bp using a Covaris sonicator. RNA-sequencing libraries were made from 600ng of sheared cDNA with the NEBNext Ultra DNA Library Prep Kit for Illumina. ~90-95M 50bp reads were obtained, per sample, on an Illumina HiSeq 2500 and analyzed using an in-house pipeline as described in Sakers et al., 2017. Briefly, reads were trimmed using Trimmomatic (v0.33), aligned to the genome using STAR (Mouse Ensembl 77) and counted with HTseq. Counts per million analyses were performed in R using the edgeR package (R Foundation for Statistical Computing, Vienna, Austria).

Gene ontology: Gene ontology analysis was performed using the BiNGO application from Cytoscape (v3.4.0). Enriched genes were identified with a Benjamini-Hochberg corrected Hypergeometric test, at a significance level of $p < 0.05$. Pre-IP genes with counts above 2 were used as a reference set for enrichment.

Patch-clamp electrophysiology—Mice were anesthetized with pentobarbital (50 mg/kg) before transcardial perfusion with ice-cold sucrose cutting solution containing the following (in mM): 225 sucrose, 119 NaCl, 1.0 NaH_2P0_4, 4.9 $MgCl_2$, 0.1 $CaCl_2$, 26.2 $NaHCO_3$, 1.25 glucose, 305 mOsm. Brains were then rapidly removed, and coronal sections 300μm thick were taken using a vibratome (Leica, VT 1200). Sections were then incubated in aCSF (32°C) containing the following (in mM): 119 NaCl, 2.5 KCl, 1.0 NaH_2P0_4, 1.3 MgCl, 2.5 $CaCl_2$, 26.2 $NaHCO_3$, 15 glucose, 305 mOsm. After an hour of recovery, slices were constantly perfused with aCSF (32°C) and visualized using differential interference contrast through a 40x water-immersion objective mounted on an upright microscope (Olympus BX51WI). Whole-cell recordings were obtained using borosilicate pipettes (3–5 MΩ) back-filled with internal solution containing the following (in mM): 130 K gluconate, 10 KCl, 10 HEPES, 10 EGTA, 2 $MgCl_2$, 2 ATP, 0.2 GTP (pH 7.35, 270-285 mOsm). Current-clamp recordings were obtained from eYFP-expressing neurons to identify spike fidelity in optogenetic stimulation. During recordings, a train of 10 action potentials were evoked through presentation of a blue LED (488nm, 1mW, 1 and 10ms pulses) at frequencies of 1, 5, 10, 20, and 60Hz. Spike fidelity was quantified as the percentage of light presentations that resulted in action potential induction. Data acquisition occurred at 10 kHz sampling rate through a MultiClamp 700B amplifier connected to a Digidata 1440A digitizer

(Molecular Devices) and were analyzed using threshold analysis in Clampfit 10.3 (Molecular Devices).

Behavior—All behaviors were performed within a sound-attenuated room maintained at 23°C at least one week after habituation to the holding room and the final surgery. For all experiments, mice were brought into the experimental behavior space and allowed to acclimate for at least 30 minutes. For all experiments, experimenters were blinded to mouse genotype or experimental manipulation. For chemogenetic and optogenetic behavior experiments, CNO dose and frequency of light stimulation were randomly assigned using block randomization, unless otherwise indicated. All pharmacological interventions (e.g. agonists and antagonists) were randomized and counterbalanced via block randomization prior to experimentation. Replication of operant responding behavior (e.g. PR test) was only used to compare experimental and control treatments with treatments counterbalanced between all mice. Sample-size estimation was determined via power analysis (G*Power 3; Faul et al., 2007) with a power of 0.85 and a standard deviation of 15-20% of the mean. Lighting was stabilized at ~1,500 lux for aversion behaviors, ~250 lux for anxiety-like behaviors. Movements were video recorded via CCD camera and analyzed using Ethovision XT 11 (Noldus Information Technologies). At the end of each study, mice were perfused with 4% paraformaldehyde followed by anatomical analysis to confirm injection sites and cell-type-specific expression.

Operant Progressive-Ratio Test—Food restricted (~90% of free feeding body weight) mice were placed in a Med-Associates operant conditioning box and subjected to magazine training during which a retractable lickometer containing a 10% sucrose solution extended for 20s at 20 random intervals for 60 minutes. Each sipper presentation was accompanied by illumination of a houselight. Following magazine training, mice were trained to nosepoke for lickometer access on a fixed ratio 1 (FR1) for 3 days (60 minutes/session). This required the mouse to nosepoke in the active nosepoke port one time to receive 20 seconds of access to the sipper. Following FR1 training, the ratio was increased to an FR3 schedule requiring the mouse to perform 3 active port nosepokes to receive access to the sipper. This schedule was used for 3 days (60 minutes/session). Finally, mice were given a progressive ratio schedule (PR) task following the geometric progression, $nj = 5e^{j/5} - 5$, in which the criteria for rewards increased in an exponential manner (1, 2, 4, 6, 9, 12…) over the training period (Richardson and Roberts, 1996). For photostimulation and photoinhibition, mice received 5 Hz or 10 Hz stimulation (473 nm, 10 ms pulse width, ~10 mW light power) and (532 nm, ~10 mW light power), respectively upon placement into the operant chamber. During all optogenetic experiments, mice were counterbalanced to receive the appropriate photostimulation or photoinhibition parameters. In photostimulation experiments, animals received 5Hz stimulation during the entire PR session, 10Hz stimulation time-locked to nosepoking during the PR session, or 10Hz stimulation time-locked to licking of sucrose reward during PR session. In photoinhibition experiments, animals received either 1 sec of illumination time-locked to nosepoking during the PR session or 1 sec of illumination time-locked to licking of sucrose reward during PR session. For chemogenetic experiments, mice received an injection of vehicle or CNO (1 mg/kg; 5 mg/kg, i.p.) 30 minutes prior to being

placed in the operant chamber on PR test day. For antagonist experiments, NOPR antagonist, J-113397 was administered (3 mg/kg, i.p.) 15 minutes prior to behavioral test.

Pavlovian Conditioning Paradigm—One week prior to Pavlovian conditioning, mice were food restricted down to ~90% of free feeding body weight. A subset of the *Pnoc*-Cre fiber photometry mice (n = 10) and *DAT-Cre* fiber photometry mice (n = 7) were trained to associate illumination of a house light (CS) with access to a sipper with 10% sucrose solution (US) within a Med-Associates operant box (ENV-307A). The house light would illuminate 6 s prior to sipper presentation. The sipper remained accessible for 20 seconds before it retracted and the house light shut off. A randomized intertrial interval of between 30-90 seconds separated consecutive trials. Pavlovian conditioning sessions lasted for 30 minutes, over which an average of 19-20 rewards were presented. For reward omission sessions, the first 10 rewards were cued and subsequently delivered as normal and every following trial only involved house light illumination with no sipper presentation. Simultaneous fiber photometry recordings were made during Pavlovian conditioning sessions as indicated in Results section. NOPR antagonist, J-113397 (3 mg/kg, i.p.) or SCH-221510 (10mg/kg, i.p.) were administered 15 minutes prior to Pavlovian conditioning.

In Vivo Fiber Photometry—Fiber photometry recordings were made throughout the entirety of 30-minute Pavlovian conditioning sessions and 1-hour FR3 and PR sessions. Prior to recording during Pavlovian or operant behavior sessions, an optic fiber was attached to the implanted fiber using a ferrule sleeve (Doric, ZR_2.5). Two LEDs were used to excite GCaMP6s. A 531-Hz sinusoidal LED light (Thorlabs, LED light: M470F3; LED driver: DC4104) was bandpass filtered (470 ± 20 nm, Doric, FMC4) to excite GCaMP6s and evoke Ca^{2+}-dependent emission. A 211-Hz sinusoidal LED light (Thorlabs, LED light: M405FP1; LED driver: DC4104) was bandpass filtered (405 ± 10 nm, Doric, FMC4) to excite GCaMP6s and evoke Ca^{2+}-independent isosbestic control emission. Prior to recording, a 120 second period of GCaMP6s excitation with 405 nm and 470 nm light was used to remove the majority of baseline drift. Laser intensity for the 470 nm and 405 nm wavelength bands were measured at the tip of the optic fiber and adjusted to ~50 μW before each day of recording. GCaMP6s fluorescence traveled through the same optic fiber before being bandpass filtered (525 ± 25 nm, Doric, FMC4), transduced by a femtowatt silicon photoreceiver (Newport, 2151) and recorded by a real-time processor (TDT, RZ5P). The envelopes of the 531-Hz and 211-Hz signals were extracted in real-time by the TDT program Synapse at a sampling rate of 1017.25Hz

Photometry Analysis—Custom MatLab scripts were developed for analyzing fiber photometry data in context of mouse behavior. The isosbestic 405 nm excitation control signal was subtracted from the 470 nm excitation signal to remove movement artifacts from intracellular Ca^{2+}-dependent GCaMP6s fluorescence (see Figure S2A). Baseline drift was evident in the signal due to slow photobleaching artifacts, particularly during the first several minutes of each hour-long recording session. A double exponential curve was fit to the raw trace and subtracted (see Figure S2B) to correct for baseline drift. After baseline correction, the photometry trace was z-scored relative to the mean and standard deviation of the hour-long session. The post-processed fiber photometry signal was analyzed in the context of

animal behavior during Pavlovian conditioning and operant task performance. Pearson correlations, one sample t-tests, two sample t-tests and two-way ANOVAs were performed using standard MATLAB functions “corr”, “ttest”, “ttest2” and “anovan”, respectively. ΔF/F was calculated as individual fluorescence intensity measurements relative to median fluorescence of entire session for 470nm channel.ΔF/F for DA cell NOPR manipulation experiments (see Figure 7) was calculated as individual fluorescence intensity measurements relative to median fluorescence of the entire vehicle treatment session. Recorded calcium dynamics were averaged into 2-second time bins and functionally categorized based on behavioral state of the animal: baseline activity during inter-trial interval, reward anticipation activity during cue presentation, or consumption activity when cue is present and animal is actively licking. A minority of scheduled FR3 and PR recording sessions were either excluded from analysis due to animal licking while sipper was retracted or not recorded due to fiber optic implant detachment before behavioral schedule was completed. 65/65 Pavlovian conditioning sessions, 33/36 planned FR3 sessions and 32/36 planned PR sessions were recorded and retained.

Real-Time Place Testing—We used custom-made unbiased, balanced two-compartment conditioning apparatus (52.5 × 25.5 × 25.5 cm) as described previously (Jennings et al., 2013; Stamatakis and Stuber, 2012). Each compartment was assigned either constant laser stimulation or no stimulation in a counterbalanced manner. Each animal was connected to a 473 nm laser via 200μm fiber optic patch cable then placed into the non-stimulation compartment at the onset of the experiment. Mice were allowed to freely roam between the two compartments for 30 minutes. Entry into the stimulation-paired compartment triggered constant photostimulation at either 5Hz, 10Hz, 20Hz or 60Hz (473 nm, 10 ms pulse width, ~10 mW light power) while the mouse remained in the stimulation-paired compartment. Entry into the non-stimulation compartment ended the photostimulation. The compartment paired with photostimulation was counterbalanced across all mice. Time spent in each compartment and total distance traveled for the entire 30-minute trial was recorder via CCD camera and measured using Ethovision 10 (Noldus Information Technologies, Leesburg, VA). Real-time preference was calculated by dividing the time spent in the stimulation-paired side by the total time in the apparatus.

Conditioned Place Preference—We used a modified three-chamber CPP apparatus consisting of two square boxes (27 cm × 27 cm) that served as the conditioning chambers separated by a small center area that served as the passageway (5 cm wide × 8 cm long) between boxes. Boxes had 2.5 cm black-and-white vertical stripes or horizontal stripes and floors were covered with 500 ml of bedding on each side. The floor of the center area was smooth Plexiglas. Mice were transported to the CPP behavior testing room and handled once per day for at least 7 days before behavioral testing. Mice were then conditioned using a semi-biased and counterbalanced CPP. On day one, mice were pretested for an initial bias to the conditioning apparatus and allowed to explore all three regions of the box drug-free for 20 minutes. Mice were paired in a counterbalanced fashion. Mice that spent >300 s on one side during the pretest were excluded due to potential side bias. Conditioning occurred over the following 2 days in which mice received a subcutaneous injection of saline in the morning and immediately confined to one side of the CPP box for 20 min. In the afternoon,

at least 4 hours after the morning conditioning session, mice received an injection of CNO (5 mg/kg, i.p.) and were immediately confined to the opposite side for 20 min. This dose of CNO has been shown to be effective in activating DREADDS. Control (vehicle-injected) mice received saline injections during both A.M. and P.M. conditioning sessions. The following day, mice were tested for a preference for the CNO-paired side following the same procedure as the pretest. Preference scores were calculated by subtracting time spent in the CNO-paired side during the pretest from time spent in the CNO-paired side during the posttest.

QUANTIFICATION AND STATISTICAL ANALYSIS

Statistical analyses—All data collected were averaged and expressed as mean ± SEM. Statistical significance was taken as *p < 0.05, **p < 0.01, and ***p < 0.001, as determined by Pearson's correlation, student's t-test, one-way ANOVA or a two-way repeated-measures ANOVA followed by Bonferroni post hoc tests as appropriate. For in situ hybridization and electrophysiology data, we used Student's t-test. For photometry experiments, we used Pearson's correlation and student's t-tests, as appropriate. For ablation, chemogenetic, and optogenetic behavioral experiments, we used one-way or two-way repeated-measures ANOVA followed by a Bonferroni post hoc tests, as described in Figures 4-6. For NOPR KO and NOPR cKO behavioral experiments, we used two-way repeated-measures ANOVA followed by a Bonferroni post hoc test, as described in Figure 7. All n values for each experimental group are described in the appropriate figure legend. For behavioral experiments, group size ranged from n = 5 to n = 18. For in situ hybridization quantification experiments, slices were collected from 4 mice, with data averaged from 3-4 slices per mouse (n = 4). For electrophysiology experiments, the number of cells recorded were as follows: n = 4 for recorded *Pnoc*-Cre^{ChR2} neurons, n = 11 for putative dopamine neurons, and n = 12 for putative non-dopamine neurons. For TRAP-RNA sequencing experiment, tissue slices were collected from 5 mice, with data averaged from 5 slices per mouse (n = 5). Statistical analyses were performed in GraphPad Prism 7.0 (Graphpad, La Jolla, CA) and MATLAB 9.1 (The MathWorks, Natick, MA).

DATA AND SOFTWARE AVAILABILITY

RNA sequencing data for pnVTA^{Pnoc} neurons from Figure 4 have been deposited and are available from GEO (Accession: GSE108813). Custom MATLAB analysis code was created to appropriately organize, process, and combine photometry recording data with associated behavioral data. Analysis code for photometry from Figure 2 and 3 is available online at: www.github.com/BruchasLab. The full behavioral data set supporting the current study are available from the corresponding author upon request.

Supplementary Material

Refer to Web version on PubMed Central for supplementary material.

Acknowledgements

This work was supported by Mallinckrodt Professorship, Hope Center for Neurological Studies (NIH P30 Blueprint Core, for Viruses), and the NIH (R37R21DA034929, 2T32DA007261-26, T32EB014856). Dougherty lab is

supported by NARSAD Independent Investigator grant from the Brain and Behavior Research Foundation, and NIH (5U01MH109133, T32GM008151). Stuber lab is supported by NIH (R37DA032750, R01DA038168 (GDS) and F32DA041184. Support also provided by the Hope Center Viral Vectors Core, and the Genome Technology Resource Center at Washington University in St. Louis (NIH P30CA91842 and UL1TR000448). We also thank Dr. Ilya Monosov (Washington University) and Dr. Paul Philips (U. Washington) for helpful insights and discussion.

References

Al-Hasani R, McCall JG, Shin G, Gomez AM, Schmitz GP, Bernardi JM, Pyo CO, Park SI, Marcinkiewcz CM, Crowley NA, Krashes MJ, Lowell BB, Kash TL,, Rogers JA, Bruchas MR (2015). Distinct subpopulations of nucleus accumbens dynorphin neurons drive aversion and reward. Neuron, 87, 1063–1077. [PubMed: 26335648]

Anton B, Fein J, To T, Li X, Silberstein L, Evans CJ (1996). Immunohistochemical localization of ORL-1 in the central nervous system of the rat. J Comp Neurol. 368(2), 229–251. [PubMed: 8725304]

Baimel C, Bartlett SE, Chiou LC, Lawrence AJ, Muschamp JW, Patkar O, Tung LW, Borgland SL (2015). Orexin/hypocretin role in reward: implications for opioid and other addictions. Br J Pharmacol, 172(2), 334–348. [PubMed: 24641197]

Beier KT, Steinberg EE, DeLoach KE, Xie S, Miyamichi K, Schwarz L, Gao XJ, Kremer EJ, Malenka RC, Luo L (2015). Circuit Architecture of VTA Dopamine Neurons Revealed by Systematic Input–Output Mapping. Cell, 162(3), 622–634. [PubMed: 26232228]

Binder EB, Kinkead B, Owens MJ, Nemeroff CB (2001). Neurotensin and dopamine interactions. Pharmacol Rev, 53, 453–486. [PubMed: 11734615]

Castro DC, & Bruchas MR (2019). A Motivational and Neuropeptidergic Hub: Anatomical and Functional Diversity within the Nucleus Accumbens Shell. Neuron, 102(3), 529–552. [PubMed: 31071288]

Ciccocioppo R, Polidori C, Antonelli L, Salvadori S, Guerrini R, Massi M (2002). Pharmacological characterization of the nociceptin receptor which mediates reduction of alcohol drinking in rats. Peptides, 23(1), 117–25. [PubMed: 11814626]

Clark JJ, Sandberg SG, Wanat MJ, Gan JO, Horne EA, Hart AS, Akers CA, Parker JG, Willuhn I, Martinez V, Evans SB, Stella N, Phillips PE (2010). Chronic microsensors for longitudinal, subsecond dopamine detection in behaving animals. Nature Methods, 7, 126–129. [PubMed: 20037591]

Danjo T, Yoshimi K, Funabiki K, Yawata S, Nakanishi S (2014). Aversive behavior induced by optogenetic inactivation of ventral tegmental area dopamine neurons is mediated by dopamine D2 receptors in the nucleus accumbens. Proc. Natl. Acad. Sci. USA, 111, 1–6.

Darland T, Heinricher MM, Grandy DK (1998). Orphanin FQ/nociceptin: a role in pain and analgesia, but so much more. Trends in Neurosciences, 21(5), 215–221. [PubMed: 9610886]

Der-Avakian A, D'Souza MS, Potter DN, Chartoff EH, Carlezon WA Jr., Pizzagalli DA, Markou A (2017). Social defeat disrupts reward learning and potentiates striatal nociceptin/orphanin FQ mRNA in rats. Psychopharmacology, 234, 1603–1614. [PubMed: 28280884]

Ewing AG and Wightman RM (1984). Monitoring the stimulated release of dopamine with in vivo voltammetry. II: clearance of released dopamine from extracellular fluid. Journal of Neurochemistry, 43, 570–577. [PubMed: 6736966]

Gan JO, Walton ME, & Phillips PE (2010). Dissociable cost and benefit encoding of future rewards by mesolimbic dopamine. Nature neuroscience, 13(1), 25. [PubMed: 19904261]

Glimcher PW (2011). Understanding dopamine and reinforcement learning: the dopamine reward prediction error hypothesis. Proc Natl Acad Sci USA, 108(3), 15647–15654. [PubMed: 21389268]

Gunaydin LA, et al. (2014). Natural neural projection dynamics underlying social behavior. Cell, 157(7), 1535–1551. [PubMed: 24949967]

Hart AS, Rutledge RB, Glimcher PW & Phillips PE Phasic dopamine release in the rat nucleus accumbens symmetrically encodes a reward prediction error term. J. Neurosci 34, 698–704 (2014). [PubMed: 24431428]

Hodos W (1961). Progressive ratio as a measure of reward strength. Science, 134(3483), 943–944. [PubMed: 13714876]

Hong S, Jhou TC, Smith M, Saleem KS, & Hikosaka O (2011). Negative reward signals from lateral habenula to dopamine neurons are mediated by rostromedial tegmental nucleus in primates. The Journal of Neuroscience, 31(32), 11457–11471. [PubMed: 21832176]

Jhou TC, Fields HL, Baxter MG, Saper CB, & Holland PC (2009). The rostromedial tegmental nucleus (RMTg), a major GABAergic afferent to midbrain dopamine neurons, selectively encodes aversive stimuli and promotes behavioral inhibition. Neuron, 61(5), 786–800. [PubMed: 19285474]

Kobayashi S, Schultz W (2008). Influence of reward delays on responses of dopamine neurons. J Neurosci 28:7837–7846. [PubMed: 18667616]

Lutfy K, Do T, Maidment NT (2001). Orphanin FQ/nociceptin attenuates motor stimulation and changes in nucleus accumbens extracellular dopamine induced by cocaine in rats. Psychopharmacology (Berl), 154(1), 1–7. [PubMed: 11291998]

Lutfy K, Eitan S, Bryant CD, Yang YC, Saliminejad N, Walwyn W, Kieffer BL, Takeshima H, Carroll FI, Maidment NT, Evans CJ (2003). Buprenorphine-induced antinociception is mediated by mu-opioid receptors and compromised by concomitant activation of opioid receptor-like receptors. Journal of Neuroscience, 23(32), 10331–10337. [PubMed: 14614092]

Madisen L, Zwingman TA, Sunkin SM, Oh SW, Zariwala HA, Gu H, Ng LL, Palmiter RD, Hawrylycz MJ, Jones AR, Lein ES, Zeng H (2010). A robust and high-throughput Cre reporting and characterization system for the whole mouse brain. Nature Neuroscience, 13(1), 133–140. [PubMed: 20023653]

Maidment NT, Chen Y, Tan AM, Murphy NP, Leslie FM (2002). Rat ventral midbrain dopamine neurons express the orphanin FQ/nociceptin receptor ORL-1. Neuroreport, 13(9), 1137–40. [PubMed: 12151756]

Matthews GA, Nieh EH, Vander Weele CM, Halbert SA, Pradhan RV, Yosafat AS, Glober GF, Izadmehr EM, Thomas RE, Lacy GD, Wildes CP, Ungless MA, Tye KM (2016). Dorsal Raphe Dopamine Neurons Represent the Experience of Social Isolation. Cell, 164(4), 617–631. [PubMed: 26871628]

McCall JG, Al-Hasani R, Siuda ER, Hong DY, Norris AJ, Ford CP, Bruchas MR (2015). CRH engagement of the Locus Coeruleus Noradrenergic System mediates Stress-Induced anxiety, Neuron, 87, 605–620. [PubMed: 26212712]

Mollereau C, Parmentier M, Mailleux P, Butour JL, Moisand C, Chalon P, Caput D, Vassart G, Meunier JC (1994). ORL1, a novel member of the opioid receptor family. Cloning, functional expression and localization. FEBS Lett, 341, 33–38. [PubMed: 8137918]

Mollereau C, Mouledous L (2000). Tissue distribution of the opioid receptor-like (ORL1) receptor. Peptides, 21(7), 907–917. [PubMed: 10998524]

Morales M, Margolis EB (2017). Ventral tegmental area: cellular heterogeneity, connectivity and behaviour. Nature Reviews Neuroscience, 18, 73–85. [PubMed: 28053327]

Mulvey B, Bhatti DL, Gyawali S, Lake AM, Kriaucionis S, Ford CP, Bruchas MR, Heintz N, Dougherty JD (2018). Molecular and Functional Sex Differences of Noradrenergic Neurons in the Mouse Locus Coeruleus. Cell Reports, 23(8), 2225–2235. [PubMed: 29791834]

Murphy NP, Maidment NT (1999). Orphanin FQ/nociceptin modulation of mesolimbic dopamine transmission determined by microdialysis. J Neurochem 73, 179–186. [PubMed: 10386969]

Namburi P, Al-Hasani R, Calhoon GG, Bruchas MR, & Tye KM (2016). Architectural representation of valence in the limbic system. Neuropsychopharmacology, 41(7), 1697. [PubMed: 26647973]

Neuhoff H, Neu A, Liss B, & Roeper J (2002). Ih channels contribute to the different functional properties of identified dopaminergic subpopulations in the midbrain. Journal of Neuroscience, 22(4), 1290–1302. [PubMed: 11850457]

Nishi M, Houtani T, Noda Y, Mamiya T, Sato K, Doi T, … & Yamashita T (1997). Unrestrained nociceptive response and disregulation of hearing ability in mice lacking the nociceptin/orphaninFQ receptor. The EMBO Journal, 16(8), 1858–1864. [PubMed: 9155012]

Norton CS, Neal CR, Kumar S, Akil H, Watson SJ (2002). Nociceptin/orphanin FQ and opioid receptor-like receptor mRNA expression in dopamine systems. J Comp Neuro, 444, 358–368.

Olszewski PK, Billington CJ, Levine AS (2000). Fos expression in feeding-related brain areas following intracerebroventricular administration of orphanin FQ in rats. Brain Research, 855, 171–175. [PubMed: 10650146]

Ozawa A, Brunori G, Mercatelli D, Wu J, Cippitelli A, Zou B, Xie XS, Williams M, Zaveri NT, Low S, Scherrer G, Kieffer BL, Toll L (2015). Knock-In Mice with NOP-eGFP Receptors Identify Receptor Cellular and Regional Localization. J Neurosci, 35(33), 11682–11693. [PubMed: 26290245]

Oliva I & Wanat MJ (2019) Operant Costs Modulate Dopamine Release to Self-Administered Cocaine. The Journal of Neuroscience 39, 1249–1260. [PubMed: 30559149]

Parker NF, Cameron CM, Taliaferro JP, Lee J, Choi JY, Davidson TJ, Daw ND, Witten I (2016). Reward and choice encoding in terminals of midbrain dopamine neurons depends on striatal target. Nature Neuroscience, 19(6), 845–854. [PubMed: 27110917]

Patriarchi, Cho JR, Merten K, Howe MW, Marley A, Xiong WH, Folk RW, Broussard GJ, Liang R, Jang MJ, Tian L (2018). Ultrafast neuronal imaging of dopamine dynamics with designed genetically encoded sensor. Science, 360 eaat4422. [PubMed: 29853555]

Pologruto TA, Yasuda R, Svoboda K (2004). Monitoring neural activity and [Ca2+] with genetically encoded Ca2+ indicators. J Neurosci. 24(43), 9572–9579. [PubMed: 15509744]

Reddy AS, O'Brien D, Pisat N, Weichselbaum CT, Sakers K, Lisci M, Dalal JS, Dougherty JD (2017). A Comprehensive Analysis of Cell Type-Specific Nuclear RNA From Neurons and Glia of the Brain. Biol Psychiatry, 81(3), 252–264. [PubMed: 27113499]

Richardson NR, Roberts DC (1996). Progressive ratio schedules in drug self-administration studies in rats: a method to evaluate reinforcing efficacy. J Neurosci Methods, 66(1), 1–11. [PubMed: 8794935]

Rodi D, Polidori C, Bregola G, Zucchini S, Simonato M, Massi M (2002). Pronociceptin/orphanin FQ and NOP receptor mRNA levels in the forebrain of food deprived rats. Brain Research, 957(2), 354–361. [PubMed: 12445978]

Russo SJ, & Nestler EJ (2013). The Brain Reward Circuitry in Mood Disorders. Nature Reviews. Neuroscience, 14(9), 609–625. [PubMed: 23942470]

Sakers K, Lake AM, Khazanchi R, Ouwenga R, Vasek MJ, Dani A, Dougherty JD (2017). Astrocytes locally translate transcripts in their peripheral processes. Proc Natl Acad Sci USA, 114, E3830–E3838. [PubMed: 28439016]

Salamone JD, Correa M, Farrar AM, Nunes EJ & Pardo M Dopamine, behavioral economics, and effort. Front. Behav. Neurosci 3, (2009).

Schultz W Dayan P Montague PR (1997) A Neural Substrate of Prediction and Reward. Science, 275, 1593–1599. [PubMed: 9054347]

Schultz W (2007). Multiple dopamine functions at different time courses. Annual Reviews in Neuroscience, 30, 259–288.

Seo D, Funderburk SC, Bhatti DL, Motard LE, Newbold D, Girven KS, McCall JG, Krashes M, Sparta DR, Bruchas MR (2016). A GABAergic Projection from the Centromedial Nuclei of the Amygdala to Ventromedial Prefrontal Cortex Modulates Reward Behavior. The Journal of Neuroscience, 36(42), 10831–10842. [PubMed: 27798138]

Shannon P, Markiel A, Ozier O, Baliga NS, Wang JT, Ramage D, Amin N, Schwikowski B, Ideker T. (2003) Cytoscape: a software environment for integrated models of biomolecular interaction networks, Genome Research, 13(11), 2498–2504. [PubMed: 14597658]

Soares-Cunha C, Coimbra B, David-Pereira A, Borges S, Pinto L, Costa P, Sousa N, Rodrigues AJ (2016). Activation of D2 dopamine receptor-expressing neurons in the nucleus accumbens increases motivation. Nat Commun, 7, 11829. [PubMed: 27337658]

Siuda ER, Copits BA, Schmidt MJ, Baird MA, Al-Hasani R, Planer WJ, Funderburk SC, McCall JG, Gereau RW, Bruchas MR (2015). Spatiotemporal control of opioid signaling and behavior. Neuron, 86, 923–935. [PubMed: 25937173]

Stamatakis AM, Stuber GD (2012). Activation of lateral habenula inputs to the ventral midbrain promotes behavioral avoidance. Nature Neuroscience, 15, 1105–1107. [PubMed: 22729176]

Stauffer W,R,, Lak A, Yang A, Borel M, Paulsen O, Boyden ES, Schultz W (2016). Dopamine neuron-specific optogenetic stimulation in Rhesus macaques. Cell, 166, 1564–1571. [PubMed: 27610576]

Stratford TR, Holahan MR, Kelley AE (1997). Injections of nociceptin into nucleus accumbens shell or ventromedial hypothalamic nucleus increase food intake. Neuroreport, 8, 423–426. [PubMed: 9080421]

Sun F, Zeng J, Jing M, Zhou J, Feng J, Owen SF, … Li Y (2018). A Genetically Encoded Fluorescent Sensor Enables Rapid and Specific Detection of Dopamine in Flies, Fish, and Mice. Cell, 174(2), 481–496.e19. [PubMed: 30007419]

Tan KR, Yvon C, Turiault M, Mirzabekov JJ, Doehner J, Labouèbe G, Deisseroth K, Tye KM, Lüscher C (2012). GABA neurons of the VTA drive conditioned place aversion. Neuron, 73, 1173–1183. [PubMed: 22445344]

Taniguchi H, et al. (2011). A Resource of Cre Driver Lines for Genetic Targeting of GABAergic Neurons in Cerebral Cortex. Neuron, 71(6), 995–1013. [PubMed: 21943598]

Tervo DG et al. (2016). A Designer AAV Variant Permits Efficient Retrograde Access to Projection Neurons. Neuron, 92(2), 372–382. [PubMed: 27720486]

Tian J, Huang R, Cohen JY, Osakada F, Kobak D, Machens CK, Callaway EM, Uchida N, Watabe-Uchida M (2016). Distributed and mixed information in monosynaptic inputs to dopamine neurons. Neuron, 91(6), 1374–1389. [PubMed: 27618675]

Toll L, Bruchas MR, Calo' G, Cox BM, & Zaveri NT (2016). Nociceptin/Orphanin FQ Receptor Structure, Signaling, Ligands, Functions, and Interactions with Opioid Systems. Pharmacological Reviews, 68(2), 419–457. [PubMed: 26956246]

van Zessen R, Phillips JL, Budygin EA & Stuber GD (2012). Activation of VTA GABA neurons disrupts reward consumption. Neuron, 73, 1184–1194. [PubMed: 22445345]

Volkow ND, Wang G-J, & Baler RD (2011). Reward, dopamine and the control of food intake: implications for obesity. Trends in Cognitive Sciences, 15(1), 37–46. [PubMed: 21109477]

Watabe-Uchida M, Zhu L, Ogawa SK, Vamanrao A & Uchida N (2012). Whole-brain mapping of direct inputs to midbrain dopamine neurons. Neuron, 74, 858–873. [PubMed: 22681690]

Witkin JM, Statnick MA, Rorick-Kehn LM, Pintar JE, Ansonoff M, Chen Y, Tucker RC, Ciccocioppo R (2014). The biology of nociceptin/orphanin FQ (N/OFQ) related to obesity, stress, anxiety, mood, and drug dependence. Pharmacol Ther 141, 283–299. [PubMed: 24189487]

Zaveri NT (2011). The Nociceptin/Orphanin FQ Receptor (NOP) as a Target for Drug Abuse Medications. Current Topics in Medicinal Chemistry, 11(9), 1151–1156. [PubMed: 21050175]

Zheng F, Grandy DK, Johnson SW (2002). Actions of orphanin FQ/nociceptin on rat ventral tegmental area neurons in vitro. Br J Pharmacol. 136(7), 1065–1071. [PubMed: 12145107]

Zhao RJ, Woo RS, Jeong MS, Shin BS, Kim DG, Kim KW (2003). Orphanin FQ/nociceptin blocks methamphetamine place preference in rats. Neuroreport, 14(18), 2383–2385. [PubMed: 14663196]

Highlights

- pnVTA^{Pnoc} neurons project locally onto VTA dopamine neurons
- pnVTA^{Pnoc} neurons become active when animals are demotivated to seek rewards
- Stimulation of pnVTA^{Pnoc} neurons reduces breakpoint and promotes avoidance behavior
- VTA dopamine neuron NOPR expression is necessary to limit reward-seeking behavior

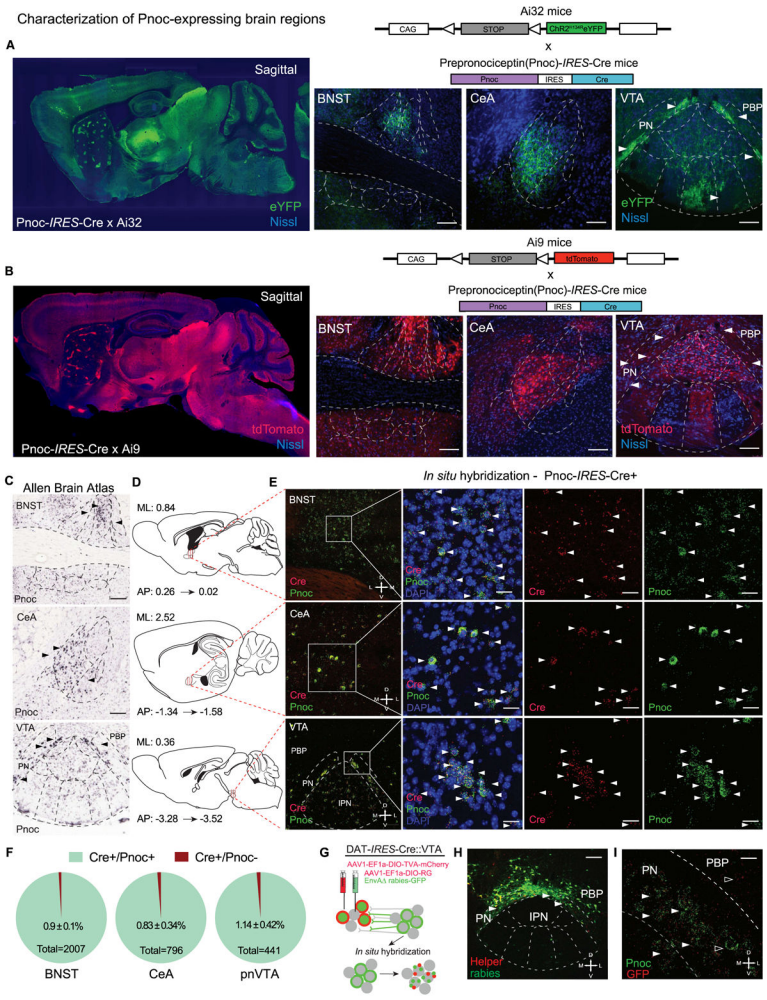

Figure 1: Anatomical Identification of Endogenous *Pnoc*-expressing VTA Inputs

(A-B) Generation of the *Pnoc*-Cre^{tdTomato} and *Pnoc*-Cre$^{ChR2/eYFP}$ mouse lines from the cross between the *Pnoc*-Cre × Ai9-tdTomato or *Pnoc*-Cre × Ai32-ChR2/eYFP. Sagittal images of *Pnoc* labeling in *Pnoc*-Cre × Ai9 or Ai32 with coronal images depicting bed nucleus of stria terminalis (BNST), central amygdala (CeA), and paranigral ventral tegmental area (pnVTA). Images show tdTomato (red) or ChR2/eYFP (green) and Nissl (blue) staining. Scale bars are 100 μm.

(C) Representative coronal images for *Pnoc in situ* hybridization from Allen Brain Institute of the BNST, CeA, VTA/IPN regions. All scale bars are 100 μm.

(D) Sagittal atlas images depicting the location of BNST, CeA, and VTA regions used for quantification.

(E) *Pnoc* and Cre expression patterns in *Pnoc*-Cre+ mice via *in situ* hybridization of *Pnoc* (green), Cre (red), and DAPI (blue) for coronal images of BNST, CeA, and pnVTA regions corresponding to panel D. Scale bars are 25 μm.

(F) Quantification of *Pnoc* expression within Cre-expressing cells in the BNST, CeA, and pnVTA (n=4, 4 mice, 3 slices each)

(G) Schematic depicting *in situ* hybridization for GFP (red) and Pnoc (green) mRNA following recombinant AAV helper viral and rabies viral injections into the VTA of DAT-Cre mice.

(H) Coronal image depicting cre-dependent helper (red) and monosynaptic rabies (green) viral expression in the VTA / IPN regions of *DAT*-Cre mice. PBP- parabrachial pigmented nucleus, PN – paranigral VTA. Scale bars are 200 μm.

(I) Coronal image depicting fluorescent *in situ* hybridization (FISH) of *Pnoc* (green) and GFP (red) colocalization in the pnVTA of *DAT*-Cre mice following recombinant AAV helper viral and rabies viral injections into the VTA. Scale bars are 25 μm.

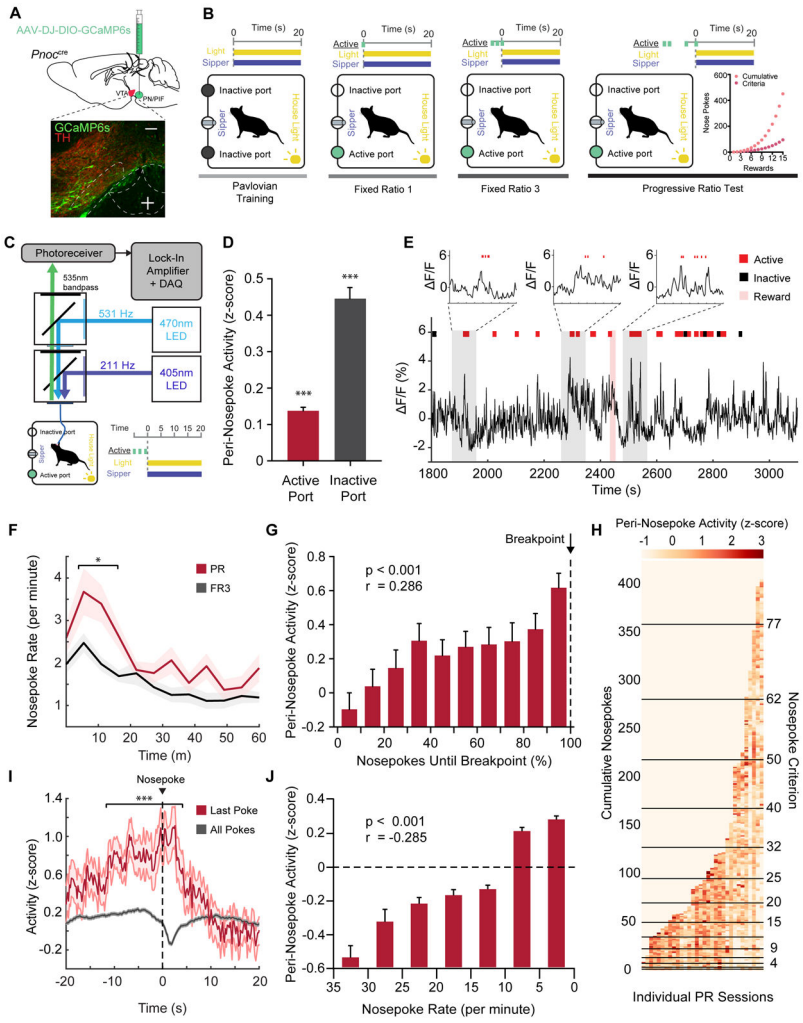

Figure 2: *Pnoc*+ VTA Inputs are Engaged During Low-Yield Reward Seeking

(A) Sagittal brain cartoon (top panel) of viral injection of GCaMP6s into the pnVTA of *Pnoc*-Cre+ mice and representative coronal image (bottom panel) showing immunohistochemistry for GCaMP6s and tyrosine hydroxylase (TH) staining. Images show GCaMP6s (green), and TH (red). Scale bars are 100 μm.

(B) Cartoon schematic depicting training regimen for Pavlovian conditioning and operant task within operant box.

(C) Cartoon schematic of fiber photometry setup for recording from mouse within operant box.

(D)Neural activity during 2 second time bins centered around active or inactive nosepoke events (n = 18 mice, 65 sessions: One sample t-test, ****p<0.001*).

(E) Representative recorded activity during PR operant task (red ticks = active nosepoke, black ticks = inactive nosepoke, red highlight = 20s reward period).

(F) Mean nosepoke rate (active nosepokes per minute) over entire hour-long FR3 sessions and PR sessions (n = 18 mice, 65 sessions: Two sample t-test, **p=0.031*).

(G) Mean peri-nosepoke activity relative to proportion of nosepokes until breakpoint for each PR session (n = 18 mice, 32 sessions: Pearson's correlation on uncategorized data points, ***$p<0.001$, $r = 0.286$).

(H) Individual 2s time bins of mean neural activity centered around active nosepoke events; shown for every active nosepoke during PR sessions (n = 18 mice, 32 sessions). Horizontal black lines indicate attainment of reward for given PR level.

(I) Mean neural activity aligned to nosepoke times for all active nosepokes and the last active nosepoke (breakpoint) for PR sessions (n = 18 mice, 32 sessions: Two sample t-test, ***$p<0.001$).

(J) Mean peri-nosepoke activity relative to nosepoke rate (active nosepokes per minute) (n = 18 mice, 32 sessions: Pearson's correlation on uncategorized data points, ***$p<0.001$, $r = -0.285$).

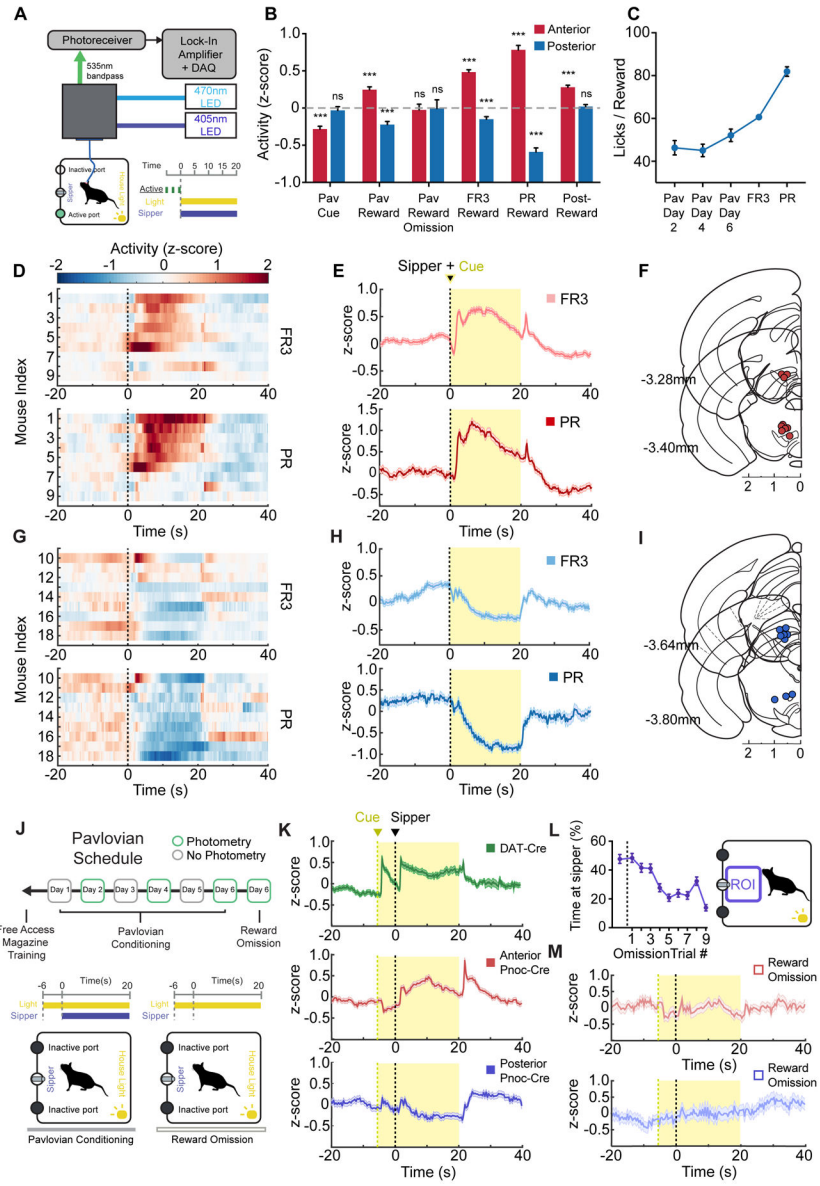

Figure 3: Anatomically Distinct Subdivisions of pnVTA^{Pnoc} Neurons are Engaged During Reward Anticipation and Consumption

(A) Cartoon schematic of fiber photometry setup.

(B) Summary of mean neural activity across various time intervals (intervals specified in Figure S3B) associated with reward anticipation and consumption during Pavlovian conditioning (n = 10 mice, 30 sessions) and operant task performance (n = 18 mice, 65 sessions; data presented as mean ± SEM; one sample t-tests: ***$p<0.001$).

(C) Number of licks per reward period during Pavlovian conditioning (n = 10 mice, 30 sessions) and operant task performance (n = 18 mice, 65 sessions; data presented as mean ± SEM).

(D) Heatmap of neural activity averaged across every reward period during FR3 (top panel) and PR (bottom panel) tasks. Each row corresponds to an individual mouse with anterior VTA fiber placement (n = 9 mice, 17 FR3 sessions, 17 PR sessions).

(E) Trace of neural activity averaged across every reward period during FR3 (top panel) and PR (bottom panel) tasks. Generated from all mice with anterior VTA fiber placement (n = 9 mice, 17 FR3 sessions, 17 PR sessions).
(F) Coronal section showing anatomical location of 400μm optic fiber implant placement for mice with anterior VTA fiber placements.
(G) Heatmap of neural activity averaged across every reward period during FR3 (top panel) and PR (bottom panel) tasks. Each row corresponds to an individual mouse with posterior VTA fiber placement (n = 9 mice, 16 FR3 sessions, 15 PR sessions).
(H) Trace of neural activity averaged across every reward period during FR3 (top panel) and PR (bottom panel) tasks. Generated from all mice with posterior VTA fiber placement (n = 9 mice, 16 FR3 sessions, 15 PR sessions).
(I) Coronal section showing anatomical location of 400μm optic fiber implant placement for mice with posterior VTA fiber placements.
(J) Pavlovian conditioning schedule and cartoon depicting time course of house light (CS) and sipper access (US) during Pavlovian conditioning.
(K) Trace of neural activity averaged across every reward period during Pavlovian conditioning. Generated from *Pnoc*-Cre mice with anterior VTA fiber placement (middle panel) (n = 5 mice, 15 sessions) and posterior fiber placement (bottom panel) (n = 5 mice, 15 sessions). Trace of neural activity also shown for *DAT*-cre mice (top panel) (n = 7 mice, 14 sessions) for comparison of DA cell and *Pnoc* cell activity over identical Pavlovian conditioning paradigm.
(L) Proportion of time spent near sipper (ROI) during reward omission periods. Data point left of dashed line represents the last rewarded trial on day 6 of Pavlovian conditioning (n = 10 mice, 10 sessions).
(M) Trace of neural activity averaged across every reward omission period during day 6 of Pavlovian conditioning. Mice with anterior VTA fiber placement (top panel) (n = 5 mice, 5 sessions) and posterior fiber placement (bottom panel) (n = 5 mice, 5 sessions).

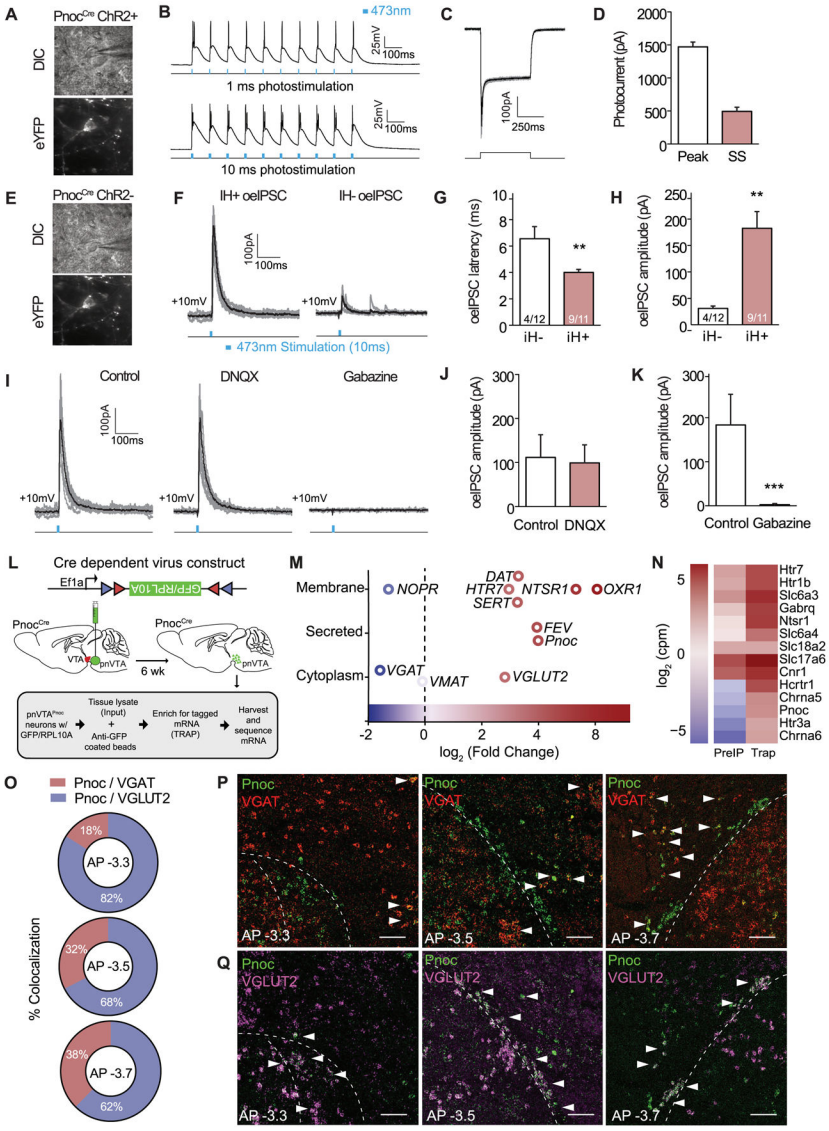

Figure 4: pnVTA^{Pnoc} Neurons Synapse onto DA Neurons and Molecularly Heterogeneous

(A) Differential interference contrast (DIC; top) and fluorescent (eYFP; bottom) images of patch recordings for *Pnoc*-Cre^{ChR2}cells.

(B) Representative traces of slice electrophysiological recordings of pnVTA *Pnoc*-Cre^{ChR2}cells following 1 and 10ms, 10Hz photostimulation.

(C) Representative traces showing photocurrent in ChR2-eYFP expressing neurons.

(D) Peak and steady-state photocurrent amplitudes in ChR2-eYFP expressing neurons (n=4).

(E) Representative images showing patch-clamp recordings from non-eYFP expressing VTA neurons.

F) Representative traces showing optically evoked inhibitory postsynaptic currents (oeIPSC) in IH+ (putative DA cells; n=11) and IH− (putative non-DA cells; n=12) neurons.

G) oeIPSC latency was faster in IH+ versus IH− neurons ($p<0.05$).

H) oeIPSC amplitude was larger in IH+ versus IH− neurons ($p<0.05$).

I) Representative traces showing oeIPSCs from VTA neurons before and after drug application.
J) oeIPSCs were unaffected by blockade of glutamate receptors.
K) oeIPSCs were abolished by blockade of GABA receptors.
(L) Cartoon depicting viral injection and TRAP of pnVTA^{Pnoc} neurons.
(M) Single-cell RNA-sequencing of TRAPed pnVTA^{Pnoc} neurons showing significantly expressed genes from membrane, secreted, and cytoplasm of *Pnoc*-labeled neurons (n=5, 5 slices per n).
(N) Heatmap from single-cell RNA-sequencing comparing Input and TRAP
(O) Pie charts depicting *Pnoc* / *VGAT* (blue) and *Pnoc* / *VGlut2* percent co-expression as a function of anterior to posterior (AP) progression (n=4, 4 slices per n).
(P) Coronal images images of *Pnoc* (green) and *VGAT* (red) mRNA expression within the pnVTA as a progression from anterior to posterior (AP). Open arrows: no colabeling and filled-in arrows: colabeling.
(Q) Coronal images of *Pnoc* (green) and *VGlut2* (purple) mRNA expression within the pnVTA from anterior to posterior (AP). Open arrows represent no co-labeling, and filled arrows represent colabeling.

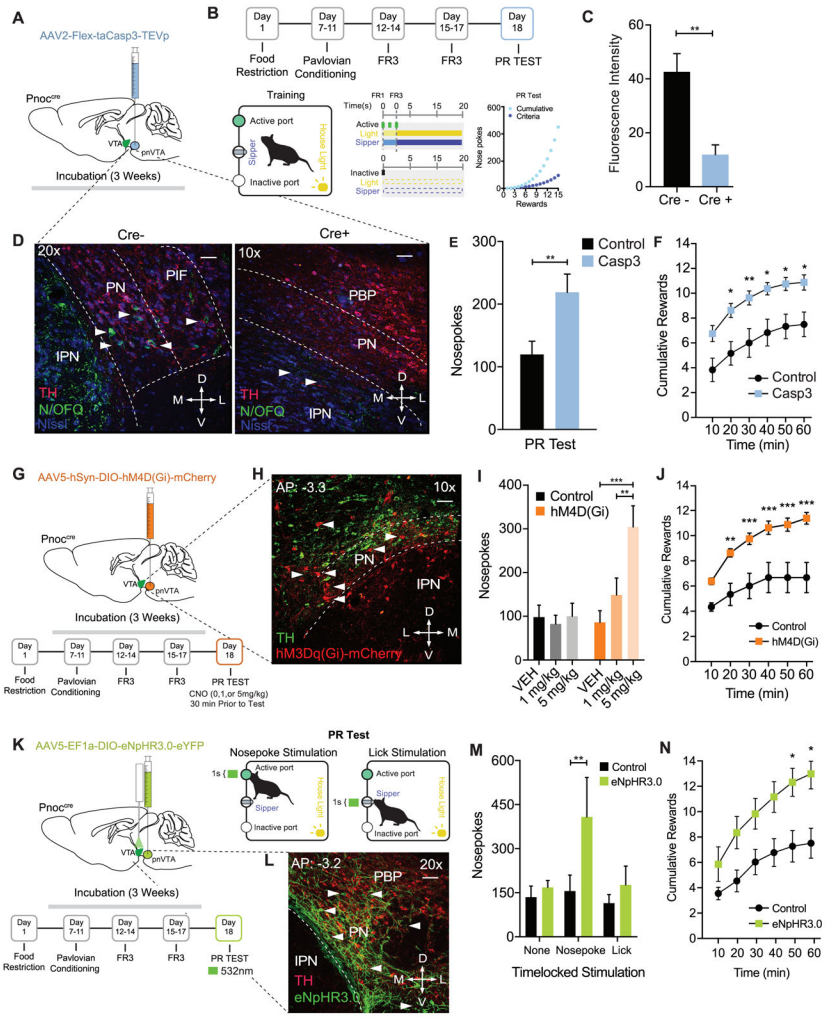

Figure 5: Selective Ablation and Inhibition of pnVTA^{Pnoc} Neurons Enhances Operant Responding for Natural Rewards

(A) Cartoon depicting injection of AAV2-FLEX-taCasp3-TEVp into the pnVTA of *Pnoc*-Cre+ and *Pnoc*-Cre− mice.

(B) Schematic and timeline for the operant training schedule, FR, and PR test days.

(C) Quantification of fluorescence intensity from immunohistochemistry analysis for N/OFQ fluorescence in *Pnoc*-Cre+ and *Pnoc*-Cre− mice following cell ablation).

(D) Representative coronal images of the VTA and IPN showing immunohistochemistry for nociceptin (N/OFQ) and tyrosine hydroxylase (TH) staining in *Pnoc*-Cre− (left panel) and *Pnoc*-Cre+ (right panel) mice. Images show N/OFQ (green), DAPI (blue) and TH (red). Scale bars are 50 and 100μm, respectively.

(E) Nosepokes performed during PR test. *Pnoc*-Cre^{taCasp3} mice have significantly increased nosepokes and rewards, compared to controls (n = 11 to 13: two-way repeated-measures ANOVA, Bonferroni post hoc; Nosepokes for control versus Casp3 during PR test $^{**}p < 0.01$,.

(F) Cumulative rewards received in Control and *Pnoc*-Cre^{taCasp3} mice. *Pnoc*-Cre^{taCasp3} mice show significantly increased number of rewards received, compared to controls (n = 11 to

13: two-way repeated-measures ANOVA, Bonferroni post hoc; Nosepokes for Control versus Casp3 during PR test *$p < 0.05$, **$p<0.01$.

(G) Calendar for injection of AAV5-hSyn-DIO-hM4D(Gi)-mCherry into the pnVTA of *Pnoc*-Cre+ and *Pnoc*-Cre− mice. Schematic and timeline for the operant training schedule and FR and PR test days.

(H) Coronal images of the pnVTA and IPN showing immunofluorescence staining tyrosine hydroxylase (TH) and hM4D(Gi)-mCherry following viral injection in *Pnoc*-Cre+ mice. Images show TH (green) and hM4D(Gi)-mCherry (red).

(I) Number of nosepokes performed during PR test. *Pnoc*-Cre$^{hM4D(Gi)}$ mice show significantly increased active nosepokes compared to Controls (n = 8: two-way repeated-measures ANOVA, Bonferroni post hoc; Nosepokes for Vehicle versus 5mg/kg, ***$p < 0.001$, 1mg/kg versus 5mg/kg **$p < 0.01$.

(J) Cumulative rewards received in Control and *Pnoc*-Cre$^{hM4D(Gi)}$ mice. *Pnoc*-Cre$^{hM4D(Gi)}$ mice receive significantly more rewards over session, compared to controls (n = 8: two-way repeated-measures ANOVA, Bonferroni post hoc; Nosepokes for control versus hM4D(Gi) during PR test, **$p < 0.01$, ***$p < 0.001$.

(K) Calendar for injection of AAV5- EF1α-DIO-eNpHR3.0-eYFP into the pnVTA of *Pnoc*-Cre+ and *Pnoc*-Cre− mice. Schematic and timeline for the operant training schedule, FR and PR test days.

(L) Coronal images of pnVTA immunofluorescence staining of tyrosine hydroxylase (TH) and eNpHR3.0-eYFP following viral injection in *Pnoc*-Cre+ mice. Images show TH (red) and eNpHR3.0-eYFP (green).

(M) Number of nosepokes performed during PR test. *Pnoc*-Cre$^{eNpHR3.0}$ mice show significantly increased active nosepokes compared to Controls following nosepoke-paired inhibition (n = 6: two-way repeated-measures ANOVA, Bonferroni post hoc; **$p<0.01$)

(N) Cumulative rewards received in Control and *Pnoc*-Cre$^{eNpHR3.0}$ mice. *Pnoc*-Cre$^{eNpHR3.0}$ mice receive significantly more rewards over session compared to control mice following nosepoke-paired inhibition (n = 6: two-way repeated-measures ANOVA, Bonferroni post hoc; Nosepoke-paired inhibition Rewards for Control versus *Pnoc*-Cre^{eNpHR3} during PR test, *$p<0.05$.

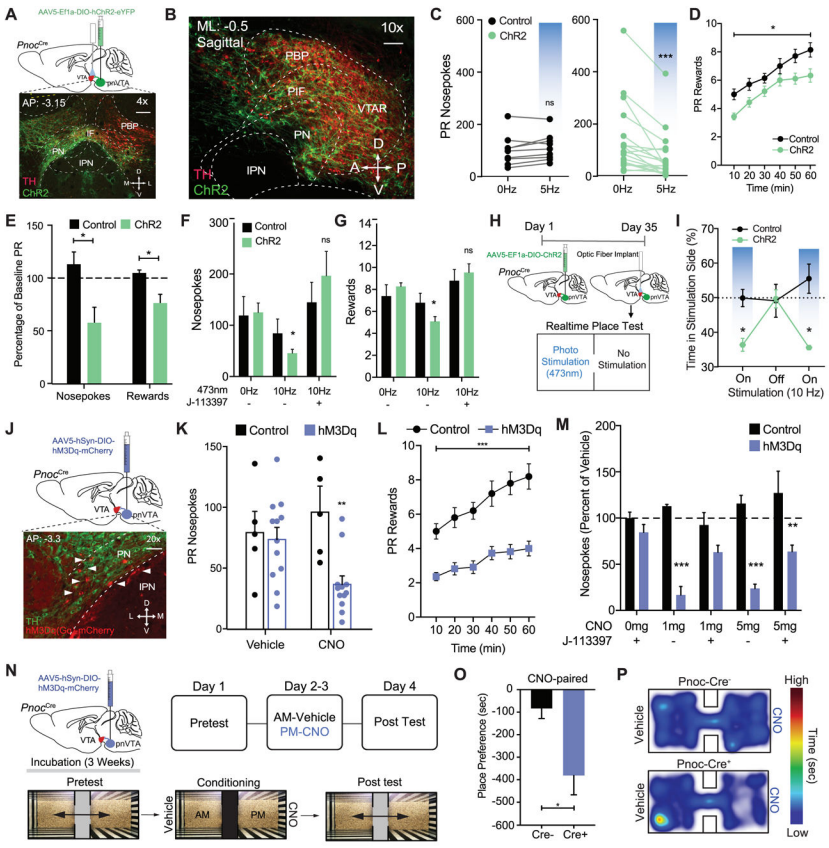

Figure 6: Optogenetic and Chemogenetic Stimulation of pnVTA^{Pnoc} Neurons Decreases Effort to Receive a Natural Reward and Promotes Aversion

(A) Sagittal brain cartoon (top) of viral injection of ChR2 into the pnVTA of *Pnoc*-Cre+ mice and representative sagittal image (bottom) showing immunohistochemistry for ChR2 (green) and tyrosine hydroxylase (TH) (red).

(B) Calendar outlining timeline and stimulation parameters for operant training schedule during FR1, FR3, and PR tasks.

(C) Number of nosepokes during PR test. *Pnoc*-Cre^{ChR2} mice decrease responding during continuous 5 Hz (10ms) blue light stimulation compared to controls (n=12: two-way repeated-measures ANOVA, Bonferroni post hoc; Nosepokes for 0Hz versus 5Hz during PR test, ***$p<0.001$).

(D) Number of rewards received over time during PR test. *Pnoc*-Cre^{ChR2} mice show a significant reduction in the number of rewards received during the PR test received following 5Hz stimulation compared to controls (n=12: Student's t-test, *$p<0.05$)

(E) Percentage of baseline nosepokes and rewards during PR test. *Pnoc*-Cre^{ChR2} mice show a significant decrease in active nosepokes and number of rewards received during 5 Hz stimulation compared to baseline and controls (n=12: One way ANOVA, Bonferroni post hoc; Nosepokes for baseline versus 5Hz during PR test *$p<0.05$, Rewards for baseline versus 5Hz during PR test *$p<0.05$).

(F) Number of nosepokes and (G) rewards during PR test in *Pnoc*-Cre^{ChR2} mice that received photostimulation (10Hz, 10ms) and the NOPR antagonist (J-113397, 3 mg/kg). *Pnoc*-Cre^{ChR2} mice show a significant decrease in active nosepokes and rewards compared

to controls during photostimulation that was rescued by treatment with J-113397 (n=12: two-way repeated-measures ANOVA, Bonferroni post hoc; *Pnoc*-Cre^{ChR2} 0Hz versus 10 Hz, **p<0.05*, 0Hz versus 10 Hz + J-113397, *ns*)

(H) Calendar outlining timeline for viral injection of ChR2 and VTA fiber optic implantation, followed by real time place testing.

(I) Time-lock (ON-OFF-ON) patterns of photostimulation-induced avoidance. Percentage of total time spent receiving 10Hz stimulation in control and *Pnoc*-Cre^{ChR2} mice (n=9 to 12: two-way repeated-measures ANOVA, Bonferroni post hoc; percentage of time spent in stimulation side for control versus *Pnoc*-Cre^{ChR2} at 10Hz **p < 0.05*).

(J) Sagittal brain cartoon (top panel) of viral injection of hM3D(Gq)-mCherry into the pnVTA of *Pnoc*-Cre+ mice and representative coronal image (bottom panel) showing immunohistochemistry for hM3D(Gq)-mCherry (red) and tyrosine hydroxylase (TH) (green).

(K) Number of nosepokes during PR test. *Pnoc*-Cre$^{hM3D(Gq)}$ mice show a significant decrease in active nosepokes CNO (5mg/kg) administration compared to controls (data presented as mean ± SEM, n=5 to 12: two-way repeated-measures ANOVA, Bonferroni post hoc; Nosepokes for baseline versus CNO (5mg/kg) during PR test ***p<0.01*) Control mice show no effect in nosepokes or number of rewards received following CNO (5mg/kg) administration.

(L) Number of rewards received over time during PR test. *Pnoc*-Cre$^{hM3D(Gq)}$ mice show a significant reduction in the number of rewards received during PR test received following CNO (5mg/kg) administration compared to controls (n=5 to 12: Student's t-test, ****p<0.001*)

(M) Number of nosepokes (as a % of vehicle treatment) during PR test in *Pnoc*-Cre$^{hM3D(Gq)}$ mice that received CNO (1 and 5 mg/kg) and J-113397 (3 mg/kg). CNO treated mice show a significant decrease in nosepokes compared to controls that was partially rescued by treatment with J-113397 (n=5 to 12: two-way repeated-measures ANOVA, Bonferroni post hoc; Nosepokes for baseline versus CNO (5mg/kg) during PR test ***p < 0.01*, Rewards for baseline versus CNO (5mg/kg) during PR test ***p < 0.01*).

N) Timeline for pnVTA viral injection and detailed calendar outlining CPP experimental paradigm.

(O) Amount of time spent on CNO-treated side during conditioned place post-test between *Pnoc*-Cre− and *Pnoc*-Cre+ mice. Post test reveals *Pnoc*-Cre$^{hM3D(Gq)}$ mice spend significantly less time in the side previously paired with CNO (5mg/kg). (n=5, 12 sessions: Student's t-test, Tukeys post-hoc, *****p<0.01*).

(P) Representative heat map of relative time spent in CPP chambers for a *Pnoc*-Cre− and *Pnoc*-Cre+ mouse during CPP post-test following 5 mg/kg CNO treatment.

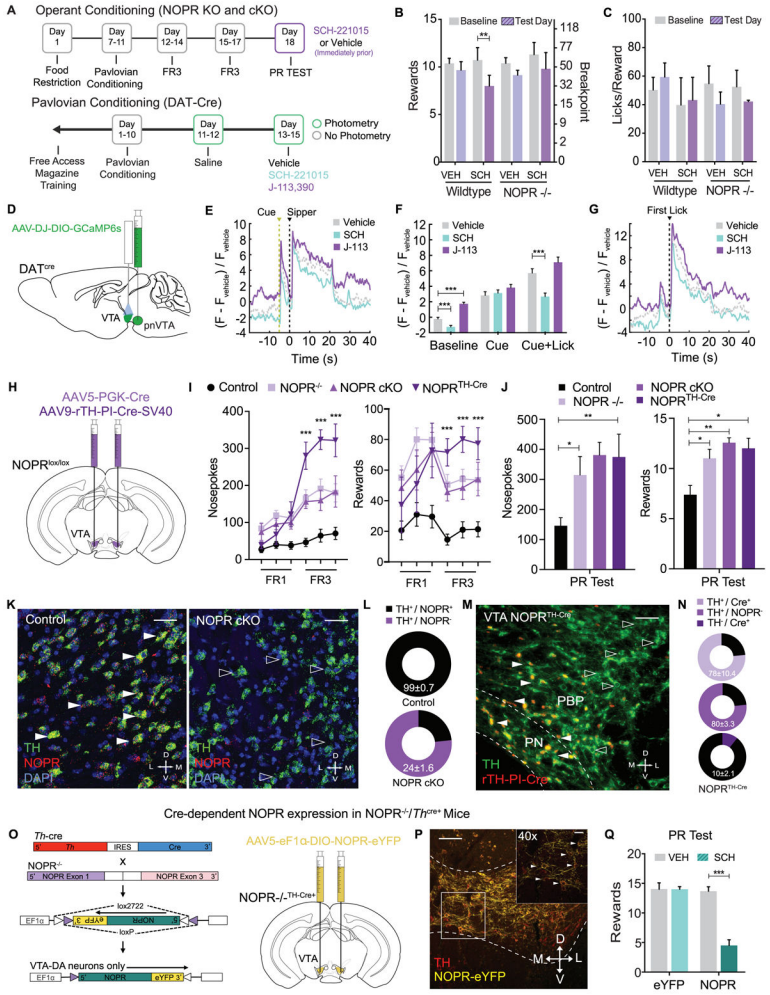

Figure 7: VTA Dopamine Neuron NOPR Expression is Necessary and Sufficient for Regulating Motivation for Sucrose

(A) Calendar outlining timeline for operant training schedule in NOPR KO and cKO experiments or pavlovian training schedule for in vivo photometry recording of *DAT*-Cre experiments.

(B) Number of rewards and licks per reward during PR test following vehicle and SCH221510 (10mg/kg) administration. Wildtype (WT) mice show a significant decrease in the number of rewards received following SCH221510 (10mg/kg) administration compared to NOPR$^{-/-}$ mice (n=6 to 8: two-way repeated-measures ANOVA, Bonferroni post hoc; Rewards for Baseline versus SCH221510 (10mg/kg) PR test $^{**}p < 0.01$).

(C) Data depicting lick rate between vehicle and SCH221510 (10 mg/kg) treated WT and NOPR KO mice during PR testing. (n=6 to 8: two-way repeated-measures ANOVA, ns).

D) Cartoon representation of viral injection of GCaMP6s in the VTA of *DAT*-cre animals.

(E) Comparison of mean DA cell dynamics across reward-predictive cue and sipper presentation in Pavlovian conditioning paradigm with systemic activation or blockade of NOPR (n=7 animals, 7 sessions per drug treatment).

(F) Activity of DA cells during Pavlovian conditioning paradigm organized into 2-s time bins based on behavioral state of animal (n=7, 7 sessions per drug treatment; data represented as mean ± SEM; two sample t-tests: ***p<0.001).
(G) Comparison of mean DA cell dynamics across first lick event within reward period of Pavlovian conditioning paradigm with systemic activation or blockade of NOPR (n = 7 , 7 sessions per drug treatment).
(H) Cartoon depicting viral conditional knock out of NOPR in the VTA of $NOPR^{loxP/YFP}$ mice after bilateral injection of AAV5-PGK-Cre or AAV9-rTH-PI-Cre-SV40 into the VTA.
(I) Number of nosepokes and rewards during FR1 and FR3 test sessions between control, NOPR KO, NOPR cKO, and $NOPR^{TH\text{-}Cre}$ mice. NOPR KO, NOPR cKO, and $NOPR^{TH\text{-}Cre}$ mice show a significant increase in the number of rewards received and total nosepokes in comparison to WT mice (n=6 to 8: two-way repeated-measures ANOVA, Bonferroni post hoc; Nosepokes and Rewards for WT versus NOPR KO, NOPR cKO, and $NOPR^{TH\text{-}Cre}$ FR1 and FR3 tests ***$p<0.001$).
(J) Number of nosepokes and rewards during PR test sessions between control, NOPR KO, NOPR cKO, and $NOPR^{TH\text{-}Cre}$ mice. NOPR KO, NOPR cKO, and $NOPR^{TH\text{-}Cre}$ mice show a significant increase in the number of rewards received and total nosepokes in comparison to WT mice (n=6 to 8: two-way repeated-measures ANOVA, Bonferroni post hoc; Nosepokes and Rewards for WT versus NOPR KO and NOPR cKO PR tests, ***$p<0.001$).
(K) Representative 40X coronal images for *in situ* hybridization showing colabeling of NOPR (red) and TH (green) mRNA in $NOPR^{lox/lox-}$ (left panel) and $NOPR^{lox/lox+}$ (right panel) mice that received injections of AAV5-PGK-Cre.
(L) Pie chart graph depicting %Co-expression of TH and NOPR mRNA in the VTA of $NOPR^{lox/lox-}$ (top panel) and $NOPR^{lox/lox+}$ (bottom panel) mice that received injections of AAV5-PGK-Cre (n=4, 4 slices per n).
(M) Representative 20X coronal images for immunofluorescence showing colabeling of Cre (red) and TH (green) in $NOPR^{lox/lox+}$ mice that received injections of AAV9-rTH-PI-Cre-SV40.
(L) Pie chart graph depicting %Co-expression of TH and Cre (top panel) and %Co-expression of TH and NOPR (bottom panel) in the VTA of $NOPR^{lox/lox+}$ mice that received injections of AAV9-rTH-PI-Cre-SV40 (n=4, 4 slices per n).
(O) Cartoon for viral rescue of NOPR in VTA dopamine cells of $NOPR^{-/-}$ X TH-Cre mice.
(P) Representative image (10x) showing NOPR-eYFP infected VTA TH^{+}-cells. Images show TH (red) and NOPR-eYFP (yellow). Inset image depicts 40x image. Arrows indicate TH and NOPR-eYFP co-labeling.
(Q) Number of rewards during PR test sessions following vehicle and SCH221510 (10mg/kg) administration. TH-Cre x $NOPR^{-/-}$ "rescue" mice show a significant decrease in the number of rewards received following SCH221510 (10mg/kg) administration compared to $NOPR^{-/-}$ mice (n=8 to 10: two-way repeated-measures ANOVA, Bonferroni post hoc; Training: Rewards for NOPR-rescue baseline PR test versus SCH221510 (10mg/kg) PR test ***$p<0.001$. No Training: Rewards for NOPR-rescue mice with Vehicle PR test versus SCH221510 (10mg/kg) PR test versus CNO (5mg/kg) during PR test ***$p<0.001$).